Local Identification of Equatorial Kelvin Waves in Real-Time Operational Forecasts

MSc Climate Physics Thesis

João Bulas Cruz

July 2023

Supervisors:

Aarnout van Delden, Utrecht University

Huib de Swart, Utrecht University

Carlos da Camara, University of Lisbon

José M. Castanheira, University of Aveiro

Department of Physics

Faculty of Science

Universiteit Utrecht

Abstract

Equatorial Kelvin waves (KWs) are associated with a variety of equatorial atmospheric phenomena. They are related to tropical convection, cloud and precipitation variability, the onset of monsoon season over Africa and India, and even equatorial oscillation patterns, namely the quasi-biennial oscillation (QBO) and the Madden-Julian oscillation (MJO). As such, if operational forecasts are to improve near the tropics, it is important that they correctly represent KWs. This thesis aims at developing a novel methodology for identifying KWs in real-time operational forecasts at specific longitudes using only the meridional structures of the solutions to the free Laplace tidal equations, known as Hough vector functions. The main advantages of this newly proposed methodology are that 1) it can univocally identify Kelvin waves at given longitudes and 2) very low computational cost is needed to apply it to real-time operational forecasts. The application of the method to 2015-2017 ECMWF analysis and operational forecast data reveals a topography related bias in the representation of the amplitude and phase of the Kelvin waves by the ECMWF operational forecast model.

Contents

1 Introduction

Equatorial Kelvin waves (KWs) belong to a broader class of geophysical fluid disturbances known as equatorial waves (EWs). EWs are planetary-scale waves in the Earth's atmosphere trapped near the equator. In general, they explain large-scale wind and pressure patterns within the tropics. They can also become coupled with convection, in which case they are responsible for modulating a substantial fraction of cloud and rainfall variability at low latitudes (Kiladis et al., 2009). As such, EWs are of special interest in the field of tropical meteorology.

Kelvin waves are no exception and, in particular, are related to the adjustment of the tropical atmosphere to convective latent heat release. They play a key role in providing momentum to the quasi-biennial oscillation (QBO) during its easterly phase (Holton and Lindzen, 1972; Plumb, 1977). Additionally, they are one of the most important EWs when it comes to explaining Madden-Julian oscillation (MJO) activity, fulfilling a crucial role in moisture convergence at the MJO convection centre (Wang et al., 2018; Castanheira and Marques, 2021). Similarly, recent connections have been found between convectively coupled Kelvin waves and tropical cyclogenisis due to the role KWs play in moisture convergence and increased convective activity (Lawton and Majumdar, 2023). Furthermore, they are often linked to the onset of monsoon season over India (Flatau et al., 2003) and Africa (Mounier et al., 2007).

Despite the importance of Kelvin waves in explaining such a wide range of equatorial atmospheric phenomena, numerical weather prediction models currently have difficulties faithfully representing them, with errors in phase speed, amplitude, and structure (Yang et al., 2009). Furthermore, over many regions, current operational forecasts of precipitation on a daily time-scale are barely better than a climatological forecast (Vogel et al., 2020). It has recently been suggested that Kelvin waves may be linked to tropical precipitation extremes, making them a potentially important source of predictability when it comes to high impact weather (Ferrett et al., 2020; Stephan et al., 2021). Thus, a coherent representation of KWs in equatorial weather forecasts is key if we are to increase model predictability near the tropics.

One of the first important works on EW theory was by Matsuno (1966), who derived the wave solutions to the shallow water equations (SWEs) for an incompressible fluid on a β-plane centered at the equator. The wave solutions were found to be of four distinct types: eastward and westward propagating inertia-gravity waves (IG), eastward propagating Kelvin waves, westward propagating Rossby waves and westward propagating mixed Rossby-gravity (MRG) waves. This categorization is due to different wave types having different restoring forces and characteristic relationships between the horizontal wind field and geopotential.

Figure 1 shows the theoretical structure of a Kelvin wave with zonal wavenumber 2. As shown by Matsuno (1966), in a β-plane approximation KWs have zero meridional velocity. They are non-dispersive and propagate with the velocity of a long gravity wave. Both gravity and Coriolis dictate the structure of the Kelvin wave: the zonal momentum is balanced by gravity and the perturbation in the surface elevation is in geostrophic balance with the zonal wind. Equatorial KWs have their maximum at and are symmetric around the equatorial line. They use the equator as an artificial boundary to propagate. This artificial boundary is created through the vanishing of the Coriolis parameter at 0^{o} latitude. Furthermore, linear wave theory postulates that, for a resting background state, KWs always propagate eastwards. Figure 2 shows a KW in the Earth's atmosphere, propagating eastwards, symmetric to the equator and using the equatorial line as a boundary to propagate.

Soon after this theoretical framework for EWs using linear wave theory was developed, observations started corroborating the existence of free Kelvin waves in the equatorial stratosphere (Yanai and Maruyama, 1966; Wallace and Kousky, 1968). Although the theory postulated the development of EWs was forced by convection events, it nevertheless assumed their development was free. It was only

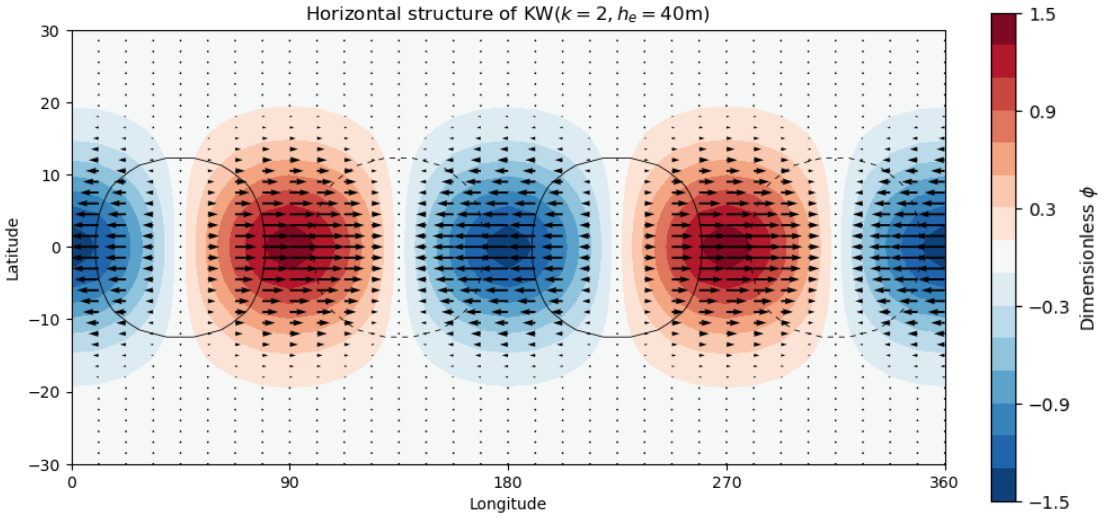

Figure 1: Horizontal structure of a Kelvin wave with zonal wavenumber $k = 2$ and corresponding to an equivalent depth $h_e = 40m$. The black arrows represent the horizontal wind field, the colour shading is according to the geopotential perturbation and the contour lines are associated to areas of mass convergence (dashed) and divergence (solid). All fields have been made dimensionless using the matrix $\mathbf{C}$ *defined as in Equation* (17).

with the advent of satellite technology in the 1970s that it became increasingly clear that EWs in general and Kelvin waves in particular could become coupled with convection in the troposphere (Wallace, 1971). To study this coupling, Takayabu (1994b,a) and Wheeler and Kiladis (1999) developed EW identification techniques based on the space–time spectral analysis of outgoing longwave radiation (OLR), a proxy for convection. By comparing the OLR power spectrum and the EW theoretical dispersion curves from linear wave theory, they were able to identify Kelvin waves, and other EW modes, where the power spectrum and theoretical dispersion curves align. Such spectral techniques, thus, were in the forefront that gave a theoretical foundation to the study of convectively coupled equatorial waves (CCEWs).

Although spectral methods are still widely used (Wong, 2009; Gehne and Kleeman, 2012), identification methods based on the projection of data onto the theoretical structures from linear wave theory have become increasingly more popular. As Yang et al. (2003) pointed out, the theoretical dispersion curves from linear wave theory, used in the space-time spectral methods, might not be valid in a more realistic background atmosphere, that is, an atmosphere that is not at rest, as Doppler shift might occur due to background winds. The alternative method developed by Yang et al. (2003, 2007, 2021) projects the data onto the theoretical structures obtained from the solutions to the SWEs on an equatorial β-plane. Such solutions are represented using parabolic cylinder functions (PCFs) and hence, the method is referred to as 2D-PCFs. The 2D-PCFs method is described in detail in the left column of Figure 3. Note that this method is usually applied univariately, without making use of the characteristic relationship between (u, v, ϕ) for each wave mode (Yang et al., 2003, 2007, 2021).

Instead of using the theoretical structures from the solutions to the SWEs on an equatorial β-plane, Žagar et al. (2005, 2009); Castanheira and Marques (2015) and Marques and Castanheira (2018) use the 3D Normal Mode Function (3D-NMFs) solutions to the linearized primitive equations over the whole sphere (Kasahara, 1976; Kasahara and Puri, 1981). The wave solutions are more accurate than the ones using PCFs and the wave types are the same: IG, MRG, Kelvin and Rossby waves. The method is outlined in the right column of Figure 3.

When compared to the 2D-PCFs method, projection onto 3D-NMFs has the advantage that no pre-

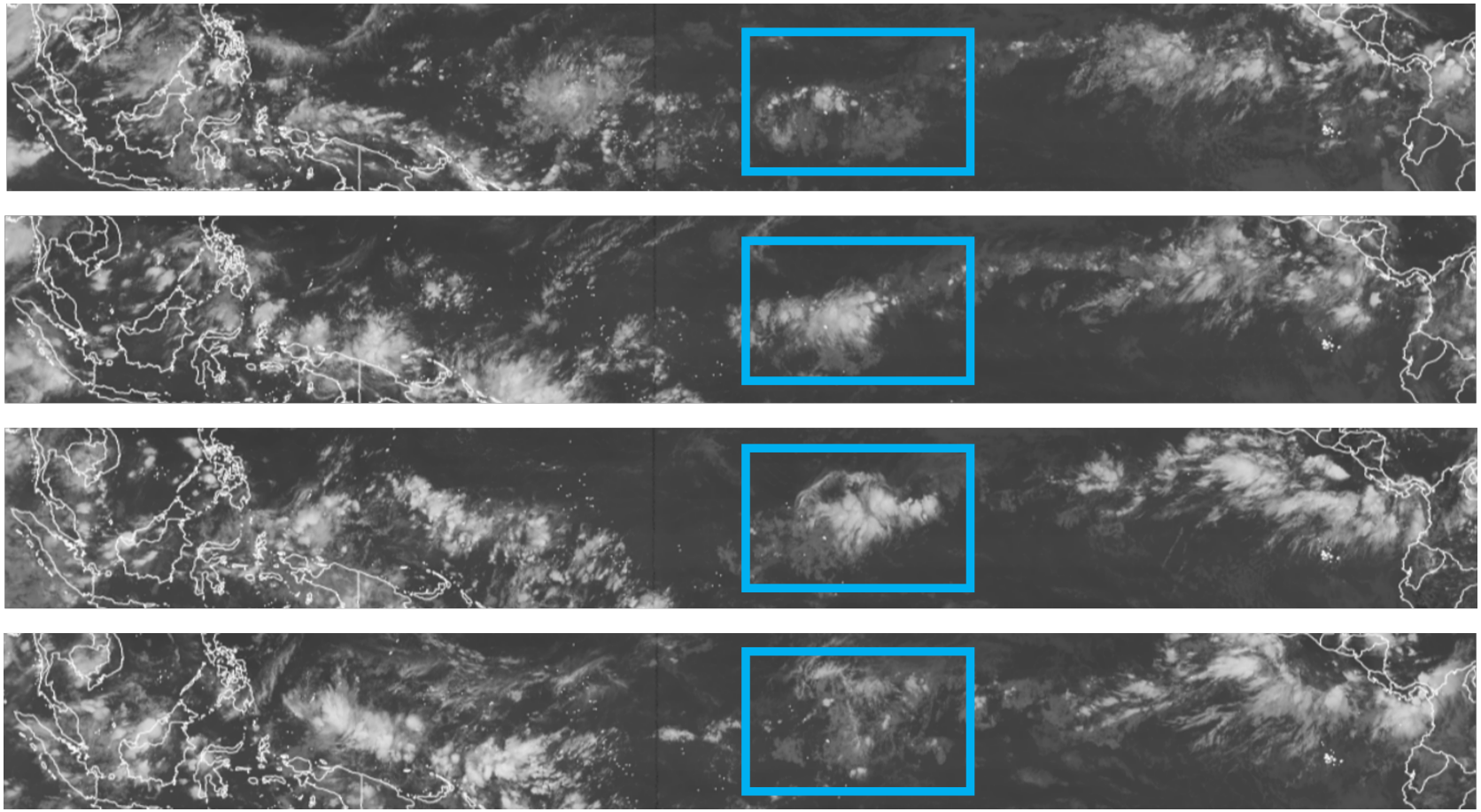

Figure 2: Unenhanced infrared satellite images of an equatorial Kelvin wave forming on 4 July 2023 09:00 (top), propagating eastwards on 5 July 2023 03:00 and 5 July 2023 18:00 (middle) and vanishing on 6 July 2023 15:00 (bottom) over the Pacific Ocean. The Kelvin wave is indicated by the blue frame. The snapshots are infrared geostationary multi-mission satellite images retrieved from EUMETSAT.

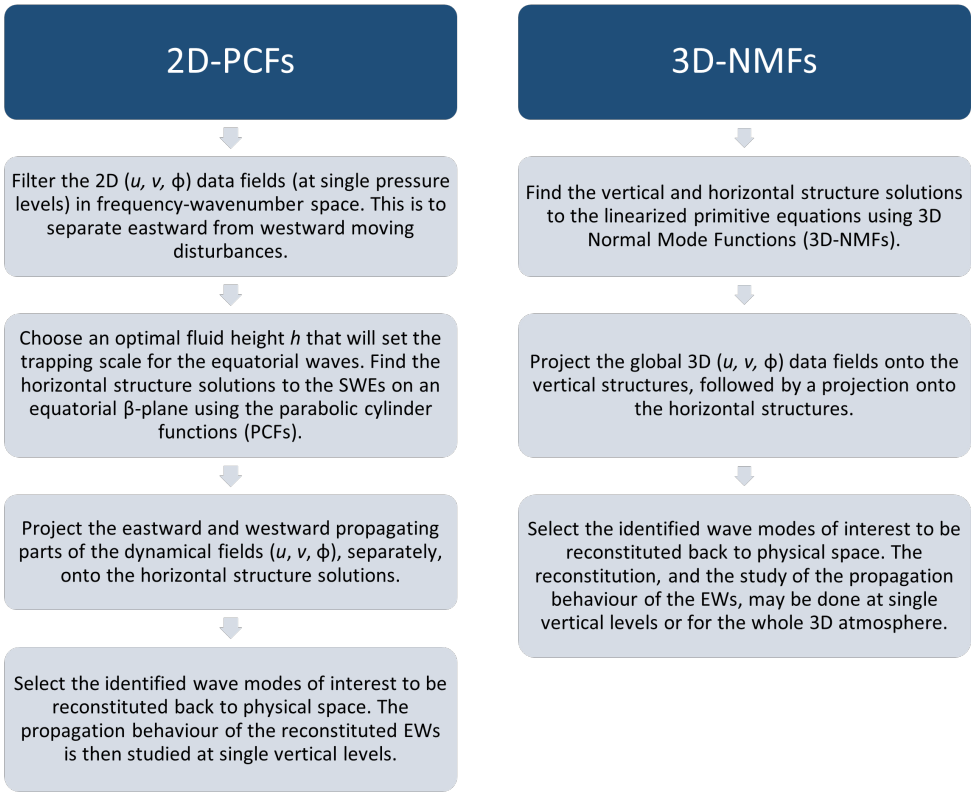

Figure 3: Flow diagram describing the steps needed to apply 2D-PCFs (left) and 3D-NMFs (right) equatorial wave identification techniques.

filtering is needed to separate eastward from westward propagating disturbances. This is because the method can univocally distinguish the wave structures by making use of the multivariate structure of the EWs. Moreover, it uses the more accurate wave solutions on the sphere instead of a β-plane approximation. However, as it is a 3D projection technique, it requires more data and computational cost to apply. Moreover, 3D NMFs are computed over an unforced and free atmosphere at rest, thus allowing for the separability between the horizontal and vertical structures to be applied. Yang et al. (2003) warns that in the presence of background winds, the horizontal and vertical structures may become coupled, making the separability assumption questionable. Although Kasahara (1980) showed that the large scale horizontal structures of the 3D NMFs do not significantly change with latitude dependent background zonal flow, there could still be vertical wind shear. Recently, to relax the separability assumption and reduce the computational power needed to apply the 3D-NMFs projection method, Castanheira and Marques (2023) have adapted the 3D-NMFs method so as to make it 2D in the horizontal, allowing it to be applied at single pressure levels, just as the 2D-PCFs technique. We will refer to this method as 2D-NMFs.

As of now, 3D and 2D-NMFs projection methods are not able to identify EWs in regional data, that is, they require data spanning the whole globe. This not only involves a higher computational cost, but might also cause problems related to the mixing of local with global signals. More precisely, a relatively local disturbance can project onto a global mode with similar horizontal scale. Thus, unrelated perturbations occurring at distinct locations in the equatorial atmosphere may project onto the same global mode, making the coherent propagation of each signal harder to capture. We note that the techniques of space-time filtering using wavelets (Wong, 2009; Roundy, 2020) and of projection onto 2D PCFs (Yang et al., 2003, 2007, 2009, 2021) are already able to identify waves at specific longitudes.

However, the former is a space-time filtering technique and not a projection method and the latter requires pre-filtering of the data onto eastward and westward moving disturbances as it is not able to univocally identify certain wave modes.

In this thesis, the goal is to develop a KW identification method, localized in longitude, that can be used to identify and diagnose KW representation in real-time operational forecasts. By doing so, the aim is to answer the following questions:

1. Would the longitudinally localized method do away with the need to pre-filter between eastward and westward moving disturbances by univocally identifying Kelvin waves?

2. Could this novel technique be applied in a real-time operational context at a low computational cost?

3. Can the localized method be used to study the phase and amplitude of Kelvin waves, thus facilitating the evaluation of KW representation by operational forecast models?

4. What results do we obtain when the methodology is applied to the 2015-2017 ECMWF operational forecast model?

With these aims in mind, the thesis is structured as follows. Section 2 is a summary of the theoretical background needed to develop the methodology. It consists of a quick overview of how the solutions to the free Laplace tidal equations can be used to study both free and convectively coupled EWs. Section 3 is concerned with the localized methodology. First, the localized KW identification technique is developed using the meridional structures of the solutions to the free Laplace tidal equations, known as Hough vectors. Then, the steps needed for the identification technique to be applicable in a real-time operational forecast context are outlined. Section 4 focuses on the application of the methodology to 2015-2017 ECMWF forecast and analysis data in order to assess the skill of the ECMWF operational forecast model at reproducing Kelvin waves.

2 Theoretical Background

2.1 Primitive Equations on the Sphere

The theory of equatorial waves as developed by Matsuno (1966) makes use of a β-plane approximation centered at the equator to describe the unforced atmosphere at rest. A more accurate representation of the atmosphere can be obtained by considering the linearized primitive equations on the sphere with diabatic forcing. In log pressure vertical coordinate z they read (Kiladis et al., 2009)

$$\frac{\partial u}{\partial t} - 2\Omega v \sin\theta + \frac{1}{a\cos\theta}\frac{\partial \phi}{\partial \lambda} = 0 \tag{1}$$

$$\frac{\partial v}{\partial t} + 2\Omega u \sin\theta + \frac{1}{a}\frac{\partial \phi}{\partial \theta} = 0 \tag{2}$$

$$\frac{1}{a\cos\theta}\left(\frac{\partial u}{\partial \lambda} + \frac{\partial (v\cos\theta)}{\partial \theta}\right) + \rho_0^{-1}\frac{\partial\left(\rho_0 w\right)}{\partial z} = 0 \tag{3}$$

$$\frac{\partial}{\partial t}\left(\frac{\partial \phi}{\partial z}\right) + N^2 w = \dot{Q}, \tag{4}$$

where ϕ is the perturbed geopotential field and (u, v, w) are the zonal, meridional and vertical components of the velocity field, respectively. The variables $(\theta, \lambda, z = -H\ln p/p_s)$ are the longitudinal, latitudinal and vertical coordinate, respectively, where p denotes pressure, p_s surface pressure and $H = R\bar{T}/g$ is the scale height for a layer mean temperature $\bar{T}$, gas constant R and mean gravity acceleration g. The reference density profile in the vertical is given by $\rho_0(z) = \rho_s \exp(-z/H)$ where ρ_s denotes the density at the surface. Constants Ω and a are the Earth's angular velocity and radius, respectively. Finally, $\dot{Q}$ is the diabatic forcing term and $N^2 = (R/H)(dT_0/dz + g/cp)$ is a measure of the static stability of the atmosphere, with dT_0/dz being the average lapse rate and c_p the specific heat of dry air at constant pressure.

2.2 Free Equatorial Waves

Free vertically propagating equatorial waves, excited by convective events in the troposphere, are known to develop in the stratosphere (Yanai and Maruyama, 1966; Wallace and Kousky, 1968). To study such waves, we need to consider the case with no diabatic forcing ($\dot{Q} = 0$) and, for simplicity, assume the static stability parameter N^2 is constant. Then Equations (1) to (4) have solutions of the form (Kiladis et al., 2009)

$$(u, v, w, \phi) = e^{z/(2H)}[\tilde{u}(\theta), \tilde{v}(\theta), \tilde{w}(\theta), \tilde{\phi}(\theta)]e^{i(k\lambda + mz - \omega t)}, \tag{5}$$

where ω is the angular frequency and (k, m) represent the zonal and vertical wavenumbers, respectively. Thus, the form of the solution given by Equation (5) corresponds to waves propagating both zonally and vertically. The factor $e^{z/2H}$ allows for the energy of the wave solution to be conserved as it compensates for the decrease in the basic state density ρ_0 with the increase in the vertical coordinate z.

Substituting the form of the solution given by Equation (5) into Equations (1) to (4) and combining Equations (3) and (4) we arrive at the free shallow water equations on the sphere, better known as the *free Laplace tidal equations*

$$-i\omega\tilde{u} - 2\Omega\tilde{v}\sin\theta + \frac{ik}{a\cos\theta}\tilde{\phi} = 0 \tag{6}$$

$$-i\omega\tilde{v} + 2\Omega\tilde{u}\sin\theta + \frac{1}{a}\frac{\mathrm{d}\tilde{\phi}}{\mathrm{d}\theta} = 0 \tag{7}$$

$$-i\omega\tilde{\phi} + \frac{gh_e}{a\cos\theta}\left(ik\tilde{u} + \frac{\mathrm{d}(\tilde{v}\cos\theta)}{\mathrm{d}\theta}\right) = 0, \tag{8}$$

where h_e is the equivalent depth which, in turn, is related to the static stability parameter through the relationship

$$N^2 = gh_e\left(m^2 + \frac{1}{4H^2}\right). \tag{9}$$

Additionally, the equivalent depth parameter h_e is responsible for setting the trapping scale of the EWs. In particular, shallower equivalent depths lead to a stronger equatorial confinement (Longuet-Higgins, 1968).

2.3 Convectively Coupled Equatorial Waves

On the other hand, in the troposphere, there are EWs forced by diabatic heating and cooling events that couple with convection (Chang, 1970; Wallace, 1971). Such convectively coupled equatorial waves (CCEWs) may be studied by assuming the diabatic forcing takes the form (Kiladis et al., 2009; Webster, 2020)

$$\dot{Q} = \epsilon N^2 w, \tag{10}$$

where ϵ is a positive constant. Note that N^2 is also positive by definition. Then, Equation (10) states that the diabatic forcing term is proportional to the static stability parameter and the vertical velocity. In particular, diabatic heating is associated to upward motion and diabatic cooling is associated to downward motion.

Using the parameterization in Equation (10), Equation (4) becomes

$$\frac{\partial}{\partial t}\left(\frac{\partial \phi}{\partial z}\right) + (1-\epsilon)N^2 w = 0 \tag{11}$$

and the form of the solution for Equations (1) to (3) and (11) is

$$(u, v, w, \phi) = Z(z)[\tilde{u}(\theta), \tilde{v}(\theta), \tilde{w}(\theta), \tilde{\phi}(\theta)]e^{i(k\lambda - \omega t)}, \tag{12}$$

where N^2 need not be constant.

Substituting back the form of the solution given by Equation (12) into Equations (1) to (3) and (11) yields, on the one hand, a vertical structure equation for $Z(z)$ and, more importantly for the purposes of this thesis, Laplace's tidal equations of the following form

$$-i\omega\tilde{u} - 2\Omega\tilde{v}\sin\theta + \frac{ik}{a\cos\theta}\tilde{\phi} = 0 \tag{13}$$

$$-i\omega\tilde{v} + 2\Omega\tilde{u}\sin\theta + \frac{1}{a}\frac{d\tilde{\phi}}{\mathrm{d}\theta} = 0 \tag{14}$$

$$-i\omega\tilde{\phi} + \frac{g(1-\epsilon)h_e'}{a\cos\theta}\left(ik\tilde{u} + \frac{\mathrm{d}(\tilde{v}\cos\theta)}{\mathrm{d}\theta}\right) = 0, \tag{15}$$

where again h_e' is the equivalent depth, only now the relationship with the static stability parameter N^2 is given by

$$N^2 = g(1-\epsilon)h_e'\left(m^2 + \frac{1}{4H^2}\right). \tag{16}$$

As to be expected, when $\epsilon = 0$, i.e. no diabatic forcing, Equation (16) is exactly the same as Equation (9). On the other hand, when $0 < \epsilon < 1$, the parameter acts to effectively reduce the static stability in the forced case when compared to the free situation, and so, Equation (16) is called the *effective static stability*. In fact, if we choose a value of ϵ close to, but less than 1, then theoretical predictions of the equivalent heights better match the observed equivalent heights of CCEWs (Gill, 1982b).

Furthermore, note that Laplace's tidal equations for the forced situation (Equations (13) to (15)) are equivalent to the free Laplace tidal equations (Equations (6) to (8)) with $h_e = (1-\epsilon)h_e'$. The difference

in this parameter has as a result that the pure gravity wave speed is reduced from $c = \sqrt{gh_e}$ in the free case to $c = \sqrt{g(1-\epsilon)h_e}$ in the forced case, making CCEWs slower than their free counterparts (Kiladis et al., 2009). More importantly, this equivalence between equations for the free and forced situations implies that the free Laplace equations can be used to study both free and convectively coupled EWs, only, for the latter, shallower equivalent depths need to be utilized to account for reduction in the effective static stability of the atmosphere.

2.4 Solutions to the Free Laplace Tidal Equations

In this subsection we will go through a quick overview of the solutions to the free Laplace's tidal equations, keeping in mind that they will allow us to study both free and convectively coupled equatorial waves. The first step is to nondimensionalize the variables $\tilde{u}(\theta), \tilde{v}(\theta)$ and $\tilde{\phi}(\theta)$, as follows

$$\mathbf{\Theta} = \begin{bmatrix} \hat{u}(\theta) \\ \hat{v}(\theta) \\ \hat{\phi}(\theta) \end{bmatrix} = \mathbf{C} \begin{bmatrix} \tilde{u}(\theta) \\ \tilde{v}(\theta) \\ \tilde{\phi}(\theta) \end{bmatrix}, \tag{17}$$

where $\mathbf{C} = \text{diag}(\sqrt{gh_e}, \sqrt{gh_e}, gh_e)$ is the nondimensionalizing matrix and the frequency is made dimensionless through $\sigma = \frac{\omega}{2\Omega}$. Then, Equations (6) to (8) can be re-written as

$$\mathbf{L\Theta} = \sigma\mathbf{\Theta}, \tag{18}$$

where $\mathbf{L}$ is given by

$$\mathbf{L} = \begin{bmatrix} 0 & i\sin\theta & \frac{\gamma k}{\cos\theta} \\ -i\sin\theta & 0 & -i\gamma\frac{\mathrm{d}}{\mathrm{d}\theta} \\ \frac{\gamma k}{\cos\theta} & -\frac{i\gamma}{\cos\theta}\frac{\mathrm{d}}{\mathrm{d}\theta}[\cos\theta(\cdot)] & 0 \end{bmatrix}, \tag{19}$$

with dimensionless parameter $\gamma = \sqrt{gh_e}/(2\Omega a)$ (Swarztrauber and Kasahara, 1985). The operator $\mathbf{L}$ is Hermitian with the inner product of two vectors $\mathbf{X}_1, \mathbf{X}_2$ defined as

$$\langle \mathbf{X}_1, \mathbf{X}_2 \rangle = \int_{-\pi/2}^{\pi/2} (\mathbf{X}_1)^* \cdot \mathbf{X}_2 \cos\theta \, d\theta, \tag{20}$$

where the asterisk $(^*)$ denotes the complex conjugate. It can be proved, as a corollary of this Hermitian property of $\mathbf{L}$, that the eigenfrequencies σ are all real, and any two eigenvectors associated to different eigenfrequencies are orthogonal (Kasahara and Puri, 1981; Swarztrauber and Kasahara, 1985).

The solutions to the eigenvalue problem given by Equation (18) are the so called Hough vector functions (Longuet-Higgins, 1968)

$$\mathbf{\Theta}^{\alpha}_{kn} = \begin{bmatrix} U(\theta) \\ iV(\theta) \\ Z(\theta) \end{bmatrix}_{kn,\alpha} \tag{21}$$

with corresponding eigenfrequencies σ^{α}_{nk} (the frequencies of the free oscillations of the atmosphere). The indices (k, n) denote the zonal and meridional wavenumber, respectively, and $\alpha = (1, 2, 3)$ distinguishes the different wave types, in ascending order: eastward IG, westward IG and Rossby.

The Hough vector functions get their name from the classical work of Hough (1897, 1898). Note that the form of the solution to the linearized primitive equations, given by Equation (5), was used to derive the free Laplace tidal equations dependent on latitude θ only (Equations (6) to (8)). However, the free Laplace tidal equations could have been written preserving their dependence on time t and longitude λ (Kasahara, 1976; Daley, 1993; Liberato et al., 2007). In this case, we would find that the full dimensionless solutions, which dictate the horizontal structure of the EWs, are of the form

$$\hat{\mathbf{W}}^{\alpha}_{kn} = e^{-i\sigma^{\alpha}_{nk}t} e^{ik\lambda} \mathbf{\Theta}^{\alpha}_{kn} \tag{22}$$

where indeed, the Hough vector functions give the latitude dependent part of the horizontal solutions and, hence, dictate the meridional structure of the equatorial waves. As such, they will be further explored in the next section to develop the localized Kelvin wave identification method.

3 Methodology

3.1 Local Identification of Kelvin Waves using Hough Vector Functions

By making use of the inner product defined in Equation (20) to generate plots similar to those in Figure 4, Castanheira and Marques (2023) analyzed the similarity between Hough modes with the same meridional and zonal wavenumbers, but corresponding to different equivalent heights. They found that for equivalent heights associated with equatorially trapped waves (approximately 10m $< h_e <$ 200m) the structure of Hough modes with low meridional wavenumber does not significantly vary. For instance, Figure 4 (a) shows that the structure of the Kelvin modes, for a wide range of zonal wavenumbers, does not change significantly for equivalent heights associated to equatorially trapped waves. Figure 1, previously shown, serves as an illustrative example of one Kelvin mode, in this case corresponding to zonal wavenumber 2, that does not significantly vary for such equivalent heights. For completeness, as Figures 4 (b)-(c) show the same as Figure 4 (a), but for the mixed Rossby gravity (MRG) modes and Rossby modes with meridional wavenumber 1 (R1), then Figures 5 (a)-(b) show the structure of one MRG mode and one R1 mode for which this is true.

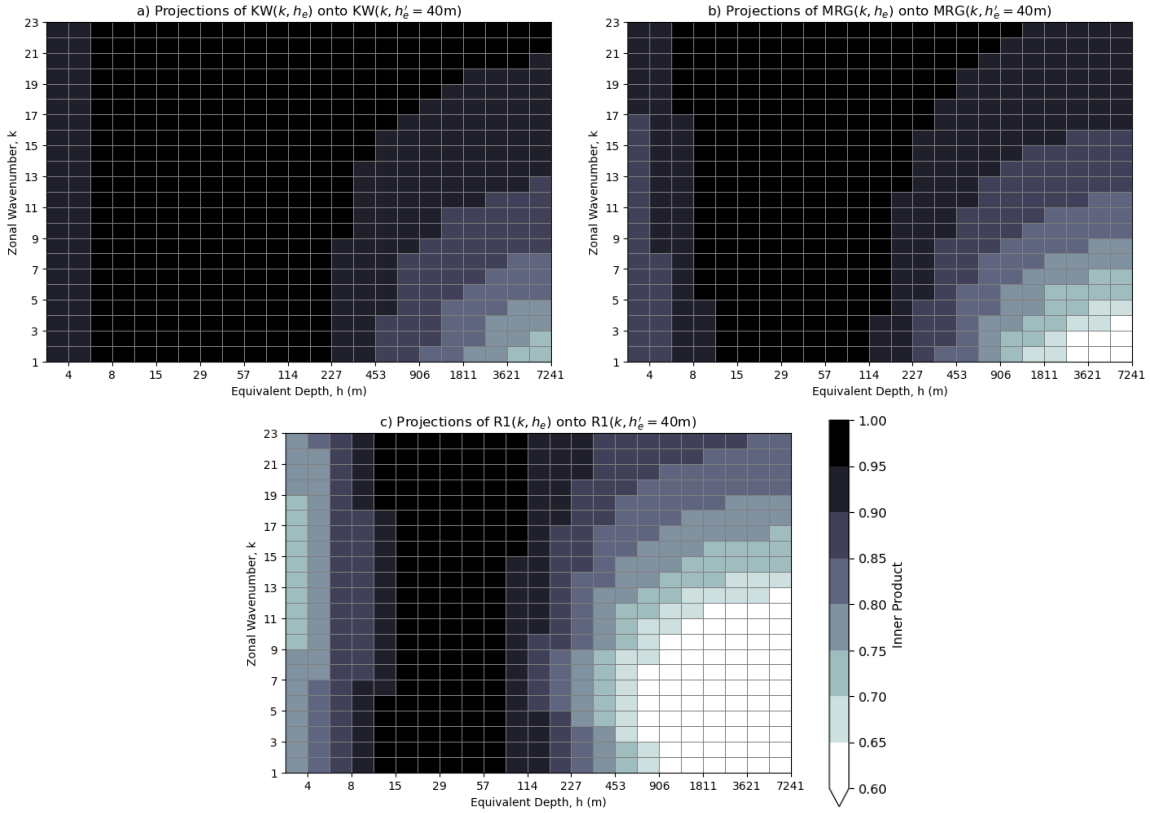

Figure 4: a) Inner product between Kelvin mode with varying equivalent height $5m \leq h_e \leq 10240m$ *and zonal wavenumber* $1 \leq k \leq 23$ *and Kelvin mode with fixed equivalent height* $h_e = 40m$ *and varying zonal wavenumber* $1 \leq k \leq 23$. *b) The same as a) only for mixed Rossby-gravity modes. c) The same as a) and b) only for the equatorial Rossby modes with meridional wavenumber* $n = 1$.

By exploiting the low sensitivity of the Hough structures to the equivalent height, the authors were able to opt for the horizontal structures of a single equivalent height ($h_e = 40$m), without making any assumptions about the vertical structure of the atmosphere. The Hough vectors of a single equivalent height are all orthogonal and their untruncated set forms a complete basis due to completeness of the Legendre polynomials (Kasahara, 1976; Kasahara and Puri, 1981). Hence, the truncated set

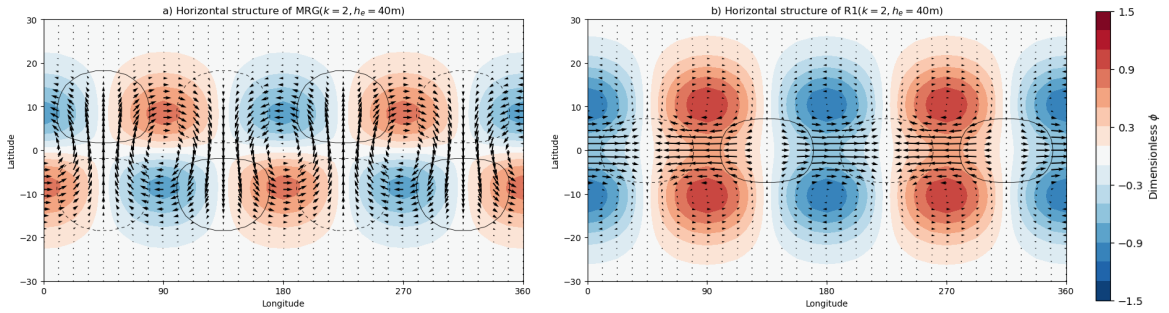

Figure 5: Horizontal structure of a) mixed Rossby-gravity wave and b) Rossby wave with meridional wavenumber $n = 2$. Both waves have zonal wavenumber $k = 2$. Both waves correspond to an equivalent depth of $h_e = 40m$, but their structure does not significantly vary for $10m < h < 200m$. The black arrows represent the horizontal wind field, the colour shading is according to the geopotential perturbation and the contour lines are associated to areas of mass convergence (dashed) and divergence (solid). All fields have been made dimensionless using the matrix $\mathbf{C}$ defined as in Equation (17).

of horizontal structure functions of a single equivalent height is a mathematically suitable basis for representing 2D horizontal atmospheric dynamics at global scales. With this in mind, let $\mathbf{W} = [u, v, \phi]^T$ be the data vector, containing data at a single pressure level. Then, the nondimensionalized data vector is given by $\hat{\mathbf{W}} = \mathbf{C}[u, v, \phi]^T$, where $\mathbf{C}$ is as in Equation (17). The 2D-NMFs method developed by Castanheira and Marques (2023) identifies EWs at single pressure levels by projecting the nondimensionalized data $\hat{\mathbf{W}}$ onto the horizontal structure functions of a single equivalent height

$$w_{kn}^{\alpha} = \int_0^{2\pi} \int_{-\pi/2}^{\pi/2} \left(e^{ik\lambda}\mathbf{\Theta}_{kn}^{\alpha}(\theta)\right)^* \cdot \hat{\mathbf{W}} \cos\theta \, d\theta \, d\lambda. \tag{23}$$

where w_{kn}^{α} are called the projection coefficients. The authors noted that, from Equation (17), the choice of the equivalent height determines the relative contribution of the geopotential, in comparison to (u, v), to the projection coefficients.

The nondimensionlized data can then be reconstituted back to physical space via the inverse transform

$$\hat{\mathbf{W}} = \sum_{n=0}^{\infty} \sum_{k=-\infty}^{\infty} \sum_{\alpha=1}^{3} w_{kn}^{\alpha}(t) e^{ik\lambda} \mathbf{\Theta}_{kn}^{\alpha}(\theta). \tag{24}$$

Indeed, as seen in Figure 6, the mean (u, v) fields of the winter (December, January, February) climatology (1990-2020) obtained from ERA5 reanalysis are very well approximated by the form of the reconstitution given by Equation (24). The reason for testing the method on a climatological mean is due to the smaller spacial scales being smoothed out, allowing us to assess how well the method reproduces the larger scales of atmospheric motion. The choice of the 200hPa pressure level is because it is one of the two standard pressure levels for studying convectively coupled equatorial waves, the other one being 850hPa. Again, as the spacial scales are usually larger at 200hPa than at 850hPa we opted for the former. Note that the reason for using these two levels as standard pressure levels for studying CCEWs lies in the fact that when there is divergence at one level there is convergence at the other, and vice-versa (Kiladis et al., 2009).

The RMSE for both u and v, in the latitude band 15°S-15°N, is approximately 1% of a standard deviation of the respective data field. As shown in Figure 7 the difference between the (u, v) data and reconstitution is mostly confined to the poles, which will not influence the ability of the method to identify equatorial waves. Overall, the 2D-NMFs technique developed by Castanheira and Marques (2023) contains a small error in the equatorial area and, thus, is concluded to be a robust EW identification method.

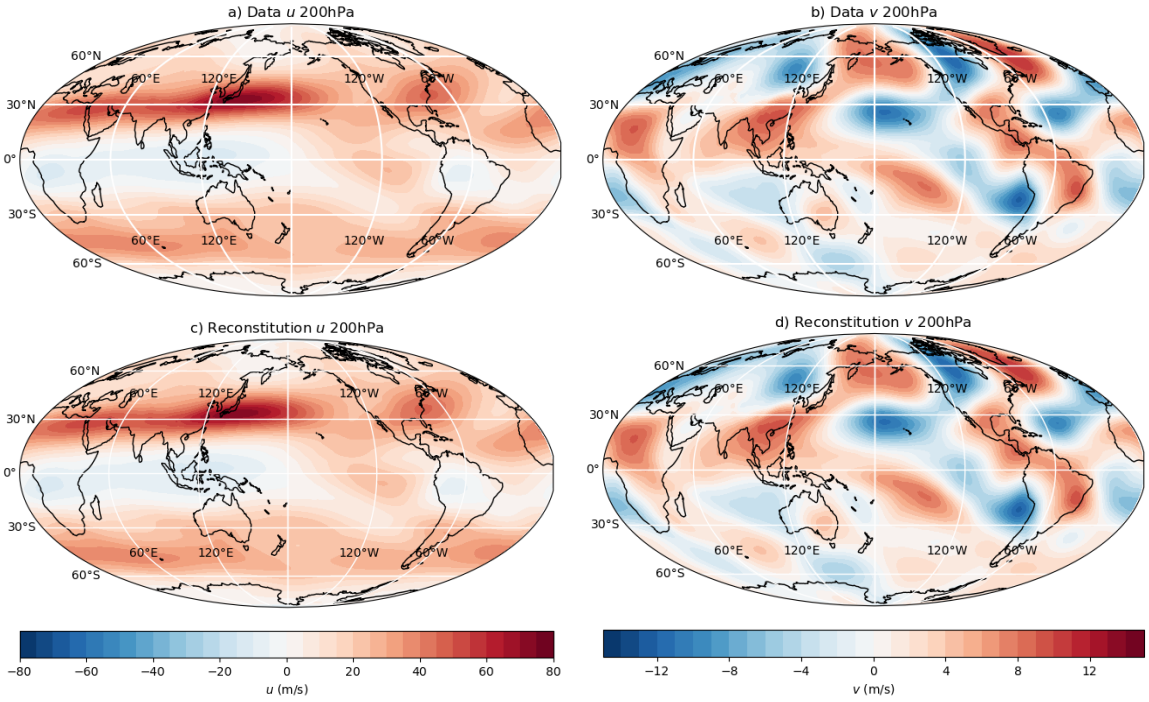

Figure 6: Mean of winter 1990-2020 climatological data for a) u and b) v at 200hPa. Reconstitution of mean winter 1990-2020 climatological c) u and d) v at 200 hPa using the method by Castanheira and Marques (2023) with an equivalent height $h_e = 40m$, number of meridional modes $N = 72$ and number of zonal modes $K = 120$.

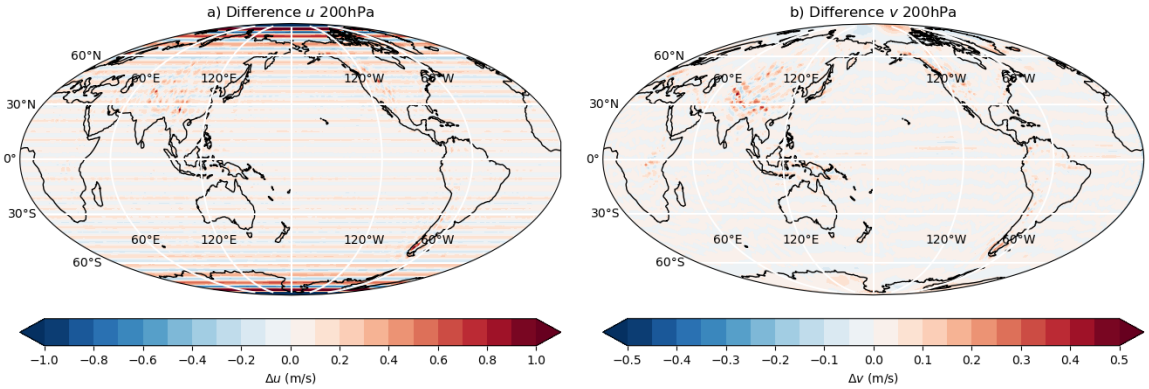

Figure 7: Difference between mean of winter 1990-2020 climatological data and reconstitution using the method by Castanheira and Marques (2023) for a) u and b) v at 200hPa with equivalent height $h_e = 40m$, number of meridional modes $N = 72$ and number of zonal modes $K = 120$.

Now, by further building on this method, the aim of this thesis is to develop a localized Kelvin wave identification technique. Let the Kelvin wave be associated to $\alpha = 1$ and $n = 0$, as is convention. Making use of the zonal wavenumber conjugate symmetry property of the Hough vectors (Swarztrauber and Kasahara, 1985; Marques et al., 2020)

$$\mathbf{\Theta}^{\alpha}_{-kn} = (\mathbf{\Theta}^{\alpha}_{kn})^*, \tag{25}$$

then the reconstitution of the dimensionless data given by Equation (24) is separated as

$$\begin{aligned}\hat{\mathbf{W}} = &\sum_{n=0}^{\infty}\sum_{k=0}^{\infty}\sum_{\alpha=1}^{3}(1-\delta_{1\alpha}\delta_{0n})\, w^{\alpha}_{kn} e^{ik\lambda}\mathbf{\Theta}^{\alpha}_{kn} \\ &+\sum_{n=0}^{\infty}\sum_{k=1}^{\infty}\sum_{\alpha=1}^{3}(1-\delta_{1\alpha}\delta_{0n})\,(w^{\alpha}_{kn})^*\, e^{-ik\lambda}\,(\mathbf{\Theta}^{\alpha}_{kn})^* \\ &+\sum_{k=0}^{\infty} w^{1}_{k0} e^{ik\lambda}\mathbf{\Theta}^{1}_{k0} + \sum_{k=1}^{\infty}(w^{1}_{k0})^* e^{-ik\lambda}(\mathbf{\Theta}^{1}_{k0})^*,\end{aligned} \tag{26}$$

i.e. as the sum over the positive zonal wavenumbers k for all non-Kelvin modes, the sum over the negative zonal wavenumbers for all non-Kelvin modes, the sum over the positive zonal wavenumbers for the Kelvin modes and the sum over the negative zonal wavenumbers for the Kelvin modes, respectively. As the non-Kelvin modes correspond to $(\alpha, n) \neq (1, 0)$, the Kronecker delta terms $\delta_{1\alpha}\delta_{0n}$ are introduced to exclude the Kelvin modes in the summations corresponding to the non-Kelvin modes.

Next, as previously mentioned, in the solutions for the β-plane approximation, the Kelvin wave has zero meridional velocity. In the case of the free Laplace tidal equations, the meridional velocity iV of the Kelvin Hough mode has a residual value. It is, however, very close to zero and thus,

$$\mathbf{\Theta}^{1}_{k0} = \begin{bmatrix} U \\ iV \\ Z \end{bmatrix}_{k0,1} \approx \begin{bmatrix} U \\ 0 \\ Z \end{bmatrix}_{k0,1} \approx \begin{bmatrix} U \\ -iV \\ Z \end{bmatrix}_{k0,1} = (\mathbf{\Theta}^{1}_{k0})^*. \tag{27}$$

As such, Equation (26) is approximated as

$$\begin{aligned}\hat{\mathbf{W}} \approx &\sum_{n=0}^{\infty}\sum_{k=0}^{\infty}\sum_{\alpha=1}^{3}(1-\delta_{1\alpha}\delta_{0n})\, w^{\alpha}_{kn} e^{ik\lambda}\mathbf{\Theta}^{\alpha}_{kn} \\ &+\sum_{n=0}^{\infty}\sum_{k=1}^{\infty}\sum_{\alpha=1}^{3}(1-\delta_{1\alpha}\delta_{0n})\,(w^{\alpha}_{kn})^* e^{-ik\lambda}(\mathbf{\Theta}^{\alpha}_{kn})^* \\ &+\sum_{k=0}^{\infty} w^{1}_{k0} e^{ik\lambda}\mathbf{\Theta}^{1}_{k0} + \sum_{k=1}^{\infty}(w^{1}_{k0})^* e^{-ik\lambda}\mathbf{\Theta}^{1}_{k0}.\end{aligned} \tag{28}$$

Figure 8 (a) shows the inner product between the $k' = 10$ Kelvin mode and all Hough modes of the same equivalent height. Figure 8 (b) is the same only for all conjugate Hough modes, which, from Equation (27) was expected to yield very similar results. Altogether, Figure 8 shows that the theoretical meridional structure of the Kelvin wave remains unchanged for different zonal wavenumbers and is orthogonal to the meridional structure of all non-Kelvin modes. There is only a small residual projection onto the $n = 2$ eastward inertia-gravity modes of high zonal wavenumber, with values always smaller than 0.1. In fact, plots using values of $k' \leq 15$ for the zonal wavenumber of the Kelvin mode yield figures very similar to Figure 8. However, as the zonal wavenumber of the Kelvin mode k' increases, the residual projections onto other non-Kelvin modes increases. For $k' > 15$ the projection onto lower order non-Kelvin modes starts becoming evident. As the lowest zonal wavenumber modes are usually the most energetic ones, this could potentially lead to problems (Kasahara and Puri, 1981;

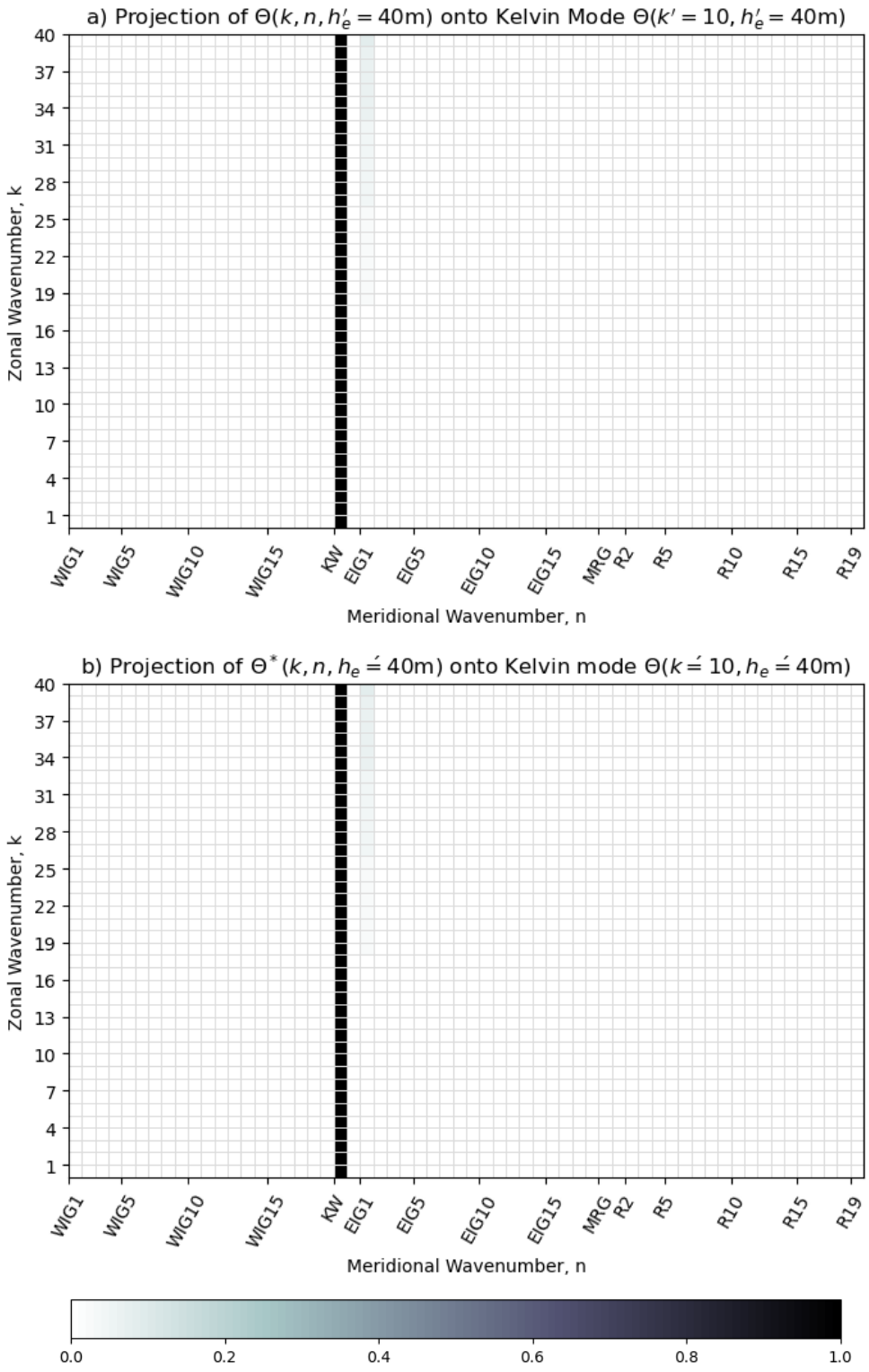

Figure 8: a) Inner product between all Hough modes with zonal wavenumber $0 \leq k < 40$ and the $k' = 10$ Kelvin mode. All modes are associated to an equivalent height $h_e = 40m$. b) The same as a) only for all conjugate Hough modes. In the x-axis an abbreviation of the Hough mode is given: westward inertia-gravity (WIG), eastward inertia-gravity (EIG), Kelvin (KW), mixed Rossby-gravity (MRG) and Rossby (R). The numbers following the abbreviation correspond to the meridional wavenumber of the Hough mode.

Tanaka, 1985; Tanaka and Kung, 1988).

In sum, this entails that, if we perform the inner product between the data vector $\mathbf{W}$ and a single Kelvin mode of zonal wavenumber $k' \leq 15$ then, to a very good approximation, all the non-Kelvin modes vanish because of orthogonality and all the Kelvin modes are preserved. In other words, performing the inner product between Equation (26) and a single $k' \leq 15$ Kelvin mode yields

$$\left\langle \hat{\mathbf{W}}, \mathbf{\Theta}^1_{k'0} \right\rangle \approx \sum_{k=0}^{\infty} w^1_{k0} e^{ik\lambda} + \sum_{k=1}^{\infty} (w^1_{k0})^* e^{-ik\lambda} = \hat{W}(t,\lambda). \tag{29}$$

So, by simply projecting the original data onto one Kelvin mode, we directly obtain a coefficient $\hat{W}(t,\lambda)$ corresponding to the amplitude of the Kelvin wave packet at each longitude and time-step. The fact that the method consists of applying one linear operation to the data and that this linear operation can be separately applied at each longitude, massively reduces the computational cost of the method, when compared to the other methodologies found in the literature.

Note that, the solutions on a β-plane, as used by Yang et al. (2003, 2021), are an approximation to the solutions to the free Laplace tidal equations. In the β-plane solutions all Kelvin modes are exactly equal to each other and all non-Kelvin modes are exactly orthogonal to the Kelvin modes i.e. there would be no residual projection onto non-Kelvin modes (Matsuno, 1966). Then, although using the solutions on a β-plane Equation (28) would be exact and not an approximation, notice that this is only the case because the β-plane solutions are an approximation in themselves.

We now give the dimensionless $\hat{W}(t,\lambda)$ coefficients velocity units by multiplying them by $c = \sqrt{gh}$. In other words, the coefficients $W(t,\lambda) = c\hat{W}(t,\lambda)$ are a proxy for the velocity of the Kelvin wave packet at each longitude and time-step. Additionally, the phase of the Kelvin waves can be studied in a straightforward manner by noticing that the field $\frac{\partial W}{\partial \lambda}$ is in quadrature with $W(t,\lambda)$ due to the $e^{ik\lambda}$ term in the form of the solution given by Equation (22). Making use of the quadrature, one can conceive of a variable in complex space

$$I(t,\lambda) = W(t,\lambda) + i\frac{\partial W}{\partial \lambda}, \tag{30}$$

whose phase is given by

$$\gamma(t,\lambda) = \arg\left(I(t,\lambda)\right) = \arctan\left(\frac{\frac{\partial W}{\partial \lambda}}{W}\right). \tag{31}$$

Since the meridional velocity of the Kelvin wave is virtually zero, $\frac{dW}{d\lambda}$ is an approximation of the mass convergence field.

Additionally, the amplitude of $I(t,\lambda)$ reads

$$A(t,\lambda) = |I(t,\lambda)| = \sqrt{W^2 + \left(\frac{\partial W}{\partial \lambda}\right)^2}. \tag{32}$$

Note that the amplitude $A(t,\lambda)$ is different from the amplitude $W(t,\lambda)$. Whereas $W(t,\lambda)$ is the amplitude of the KW packet and thus, is only related to the wind/geopotential, $A(t,\lambda)$ is the amplitude of the complex variable $I(t,\lambda)$ and thus, incorporates both the wind/geopotential and the mass divergence field. Although most of the analysis of the operational forecast model will be done using the amplitude of the Kelvin wave packet $W(t,\lambda)$, the amplitude $A(t,\lambda)$ of the complex variable will prove useful in certain instances (such as the amplitude-phase plots in Figure 15).

3.2 Real-Time Application to Operational Forecasts

The purpose of this subsection is to develop a framework that allows for the application of the localized Kelvin wave identification technique in real-time operational forecasts, so as to assess the model's skill at reproducing KWs.

The first step is to apply a frequency filter to the $W(t, \lambda)$ coefficients. As the aim is to evaluate the skill of short term forecasts, up to 10 days, we are not concerned with their skill at reproducing very low frequency waves, that is, waves with periods corresponding to seasonal scales or larger. We are not interested in diurnal cycles or noise either. Furthermore, for completeness, if we want to remove certain wavenumbers, a spacial filter may also be applied. To achieve these purposes we choose to employ a Lanczos bandpass frequency filter that only preserves waves with periods between 2-30 days and we choose to remove the zonal mean. The choice of the Lanczos filter over other possibilities is due to its ability to reduce the Gibbs phenomena. For a more detailed and theoretical discussion on Lanczos filters see Duchon (1979) and Hamming (1983).

Moreover, as the method is to be applied in a real-time operational context, using very large time windows would make the methodology obsolete. To choose a window size that is small enough for the method to be operationally usable, but also large enough for the error in the frequency filter to be small, we compare the RMSE of applying the frequency filter to different size windows. The RMSE shown in Figure 9 is calculated by comparing the different window sizes to a 180-day window which should introduce a negligible error using the chosen filter. Figure 9 then shows that, for both pressure levels, a 90-day window would have an average RMSE of $\sim 7.5\%$ of one standard deviation. We will opt for this window size, although a window size of 60 days would still be an acceptable choice with the average RMSE only being $\sim 13\%$ of one standard deviation, for both pressure levels.

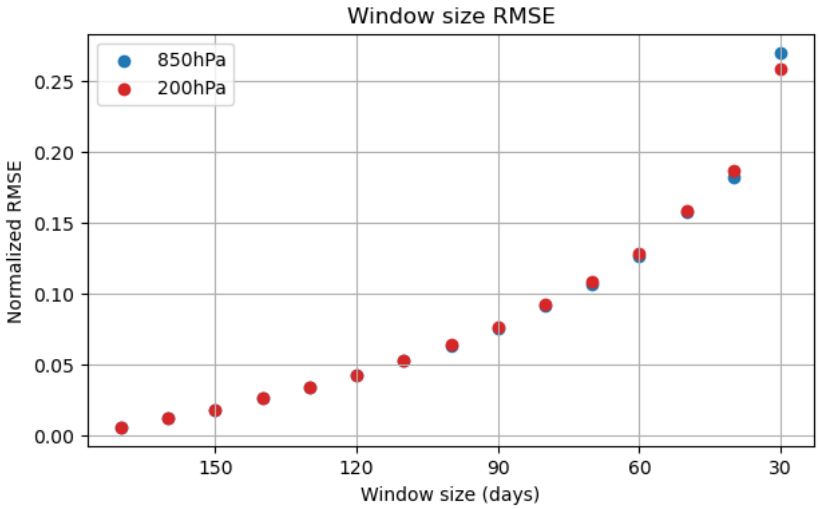

Figure 9: Normalized RMSE from applying the frequency filter to the $W(t, \lambda)$ coefficients using different size windows, for 850hPa and 200hPa. All window sizes are compared to an 180-day window. The RMSE is normalized by the standard deviation in the 180-day window. The $W(t, \lambda)$ coefficients were obtained using daily (u, v, ϕ) ERA5 data for the year 2016.

Having made the choice of using a 90-day window, we now want to create 3 different types of 90-day windows so as to better assess the skill of numerical weather prediction models: the diagnostic dataset, the perfect forecast dataset and the real-time forecast dataset. As shown in Figure 10 the diagnostic dataset consists only of analysis data and the window is centered, i.e. the frequency filter is applied at the center of the window. The perfect forecast dataset is only made up of analysis data only, as well, however, it is off-centered and thus, allows for quantifying the error originating from the Lanczos filter

being applied at the edge of the window, which we will refer to as *edge effects*. The real-time forecast dataset consists of 80 days of analysis data with 10 days of forecasts appended at the end, allowing for the study of model error. As this last window type is off-centered it also contains edge effects on top of the model error. The nomenclature adopted is as in Yang et al. (2021).

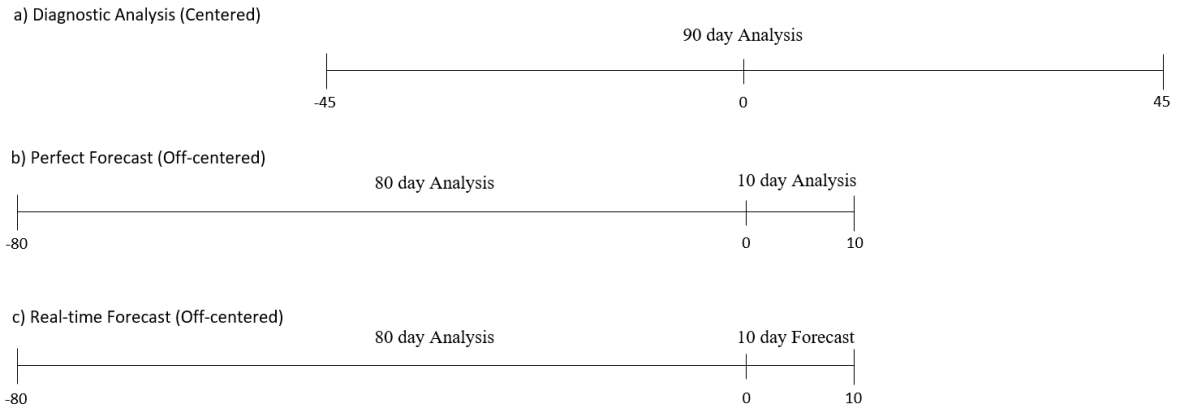

Figure 10: Schematic of the three 90-day window types used as input for the Lanczos frequency filter. a) Diagnostic analysis dataset: consists of 90 days of analysis data and the filter is applied at the center of the window. b) Perfect forecast dataset: consists of 90 days of analysis data and filter is applied at the edge of the window. c) Real-time forecast dataset: consists of 80 days of analysis with 10 days of forecast data appended at the end and filter is applied at the edge of the window. Adapted from Yang et al. (2021).

As schematized in Figure 11, if we compare the perfect forecast dataset to the diagnostic dataset the edge effects from the frequency filter will be visible. On the other hand, when comparing the real-time forecast to the perfect forecast dataset, we are studying the model error. Finally, if the real-time forecast is compared to the diagnostic dataset, both the model error and the edge effects are present. In sum, the comparison between the different window types allows us to study and isolate the different error types, which may arise from the model or the edge effects of the frequency filter.

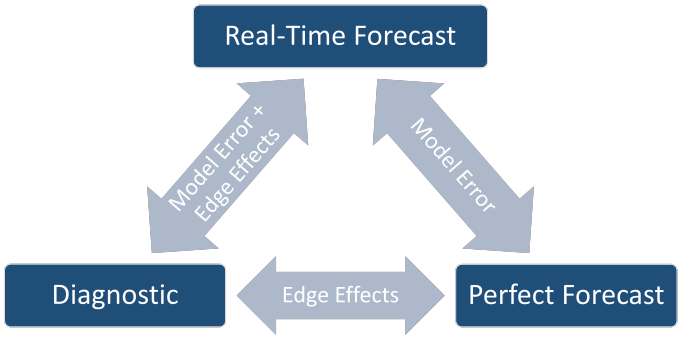

Figure 11: Scheme showing which error is studied when two given window types are compared.

3.3 Method Summary

The application of the method to real-time operational forecasts consists in the following steps:

1. Nondimensionalize the data $\mathbf{W} = [u, v, \phi]^T$ using

$$\hat{u} = \frac{u}{\sqrt{gh_e}}, \quad \hat{v} = \frac{v}{\sqrt{gh_e}}, \quad \hat{\phi} = \frac{\phi}{gh_e}. \tag{33}$$

2. Apply the Kelvin wave identification technique by projecting the dimensionless data onto one Kelvin mode with $k' \leq 15$

$$\hat{W}(t,\lambda) = \left\langle \hat{\mathbf{W}}, \mathbf{\Theta}^1_{k'0} \right\rangle, \tag{34}$$

where $\hat{\mathbf{W}}$ is the dimensionless data vector and $\mathbf{\Theta}^1_{k'0}$ is the chosen Kelvin mode.

3. Arrange the dimensionless Kelvin wave amplitude coefficients $\hat{W}(t,\lambda)$ in the three 90-day window types: diagnostic, perfect forecast and real-time forecast.

4. Give the dimensionless Kelvin wave amplitude coefficients $\hat{W}(t,\lambda)$ velocity units via

$$W(t,\lambda) = \hat{W}(t,\lambda)\sqrt{gh_e}, \tag{35}$$

making $W(t,\lambda)$ a proxy for the zonal velocity.*

5. Apply frequency and wavenumber filters to $W(t,\lambda)$ as desired.

6. Making use of the filtered wave amplitude coefficients $W(t,\lambda)$, create the complex variable

$$I(t,\lambda) = W(t,\lambda) + i\frac{\partial W}{\partial \lambda}. \tag{36}$$

Then, the amplitude and phase at each longitude and time, can be obtained via

$$A = |I(t,\lambda)| \quad \text{and} \quad \gamma(t,\lambda) = \arg\left(I(t,\lambda)\right), \tag{37}$$

respectively.

7. Assess the skill of the operational forecast model at representing Kelvin waves using the filtered $W(t,\lambda)$, $A(t,\lambda)$ and $\gamma(t,\lambda)$.

* Note that if we were to multiply the dimensionless $\hat{W}(t,\lambda)$ by gh_e we would instead obtain a proxy for the geopotential perturbation ϕ.

3.4 Data

European Centre for Medium-Range Weather Forecasts (ECMWF) analysis and real-time operational forecast 6-hourly data is used, spanning the entirety of the years 2015 - 2017. The horizontal wind components (u, v) and the geopotential height ϕ at the 850hPa and 200hPa pressure levels are regridded onto a regular 1° latitude x 1° longitude grid before being projected onto the chosen Kelvin mode.

ECMWF forecast and analysis data is produced using the Integrated Forecasting System (IFS). During the period studied, the IFS stayed consistent, having only gone through some minor changes. In the beginning of 2015 the cycle 40r1 was in use. Then, an upgrade in the horizontal resolution to better resolve physical processes and increase the energy at the finer scales was implemented on 8 March 2016, with cycle 41r2. Afterwards, the coupled dynamical ocean model (NEMO) increased its resolution from 1 degree and 42 layers to 0.25 degrees and 75 layers with cycle 43r1, on 22 November 2016. Finally, on 11 July 2017, cycle 43r3 was implemented, bringing changes in data assimilation and an improved scheme for simulating convection.

4 Results and Discussion

The methodology outlined in Section 3.3 is now applied to the 2015-2017 ECMWF analysis and forecast data described in Section 3.3. By doing so, the ECMWF 2015-2017 forecast model skill at representing Kelvin waves is evaluated.

4.1 Kelvin Wave Propagation

Figure 12 shows the Hovmöller diagrams of the KW amplitude $W(t, \lambda)$, defined as in Equation (35) for the year 2016 at 850hPa (top row) and 200hPa (bottom row) for the different window types: diagnostic, perfect forecast and real-time forecast. As previously mentioned, a Lanczos filter has been applied to the $W(t, \lambda)$ coefficients that preserves waves with periods 2-30 days and their zonal mean has been removed. According to linear wave theory, for a resting background state, Kelvin waves travel eastwards, and that is the case for most Kelvin waves seen at both levels in Figure 12. However, no pre-filter was applied to separate eastward from westward moving disturbances in the data and the method is able to identify Kelvin waves travelling westward. One such example is seen at 850hPa in Figures 12 (a)-(c) during the period from mid-October until early November, when Kelvin waves are travelling from $\sim 135°$E to $\sim 90°$E. Although we will not delve into the reasons for the westward propagation of some of the identified KWs, it is important to note that this is indeed possible, as there exist mechanisms known to change the velocity and direction of travel of equatorial waves in general. One possible mechanism is the Doppler shift suffered by EWs in the presence of a nonzero zonal mean flow (Yang et al., 2003).

The most prominent difference between the Hovmöller diagrams at 850hPa (top row) and 200hPa (bottom row) is that no clear discontinuities in wave propagation are seen at 200hPa. At 850hPa the longitudes 35^{o}E and 280^{o}E are clearly visible as cut-off regions when it comes to wave propagation. These longitudes correspond to regions of high topography at the equator that reach the 850hPa level but never the 200hPa level, as shown in Figure 13. This is why the discontinuities are only visible at 850hPa. ECMWF data is extrapolated below the surface using hydrostatic balance for the geopotential field and by keeping the surface velocity constant below ground for the (u, v) fields (Yessad, 2015). This means the characteristic structure between the horizontal velocity and geopotential fields is lost, making it highly unlikely that Kelvin waves would be identified by the method in data extrapolated below the surface. Therefore, we attribute the discontinuities at longitudes corresponding to high topography seen in at 850hPa to physical phenomena, that is, the topographic effects present in the development and propagation of Kelvin waves.

Figure 14 shows the difference plots resulting from the comparison of the Hovmöller diagrams shown in Figure 12. Again, the top row shows the results for 850hPa and the bottom row for the 200hPa pressure level. The left column of Figure 14 corresponds to the difference between the real-time and diagnostic datasets and, hence, shows the edge effects of the frequency filter. This difference is very small in magnitude and mainly affects the lower frequency waves. Moreover, the difference between the real-time and perfect forecast for lead day 2 is shown in the middle column of Figure 14, corresponding to model error. As model error is confined to certain longitude ranges, that indicates it is less related to the frequency of the waves, and more closely linked to their zonal wavenumber. More specifically, at 850hPa three crests and three troughs can be seen throughout the longitude axis, indicating errors in the reproduction of wavenumber 3. At 200hPa it is harder to distinguish, however at least two crests and two troughs are visible, suggesting difficulty of the model in reproducing wavenumbers close to wavenumber 2. In sum, model error seems to primarily affect the low zonal modes. Finally, the rightmost column of Figure 14 shows the difference between the real-time forecast for lead day 2 and the diagnostic dataset, thus containing both model error and edge effects. It is seen that the rightmost plots are very similar to the middle column plots, thus, corroborating that model error has a much larger magnitude than the edge effects arising from the frequency filter.

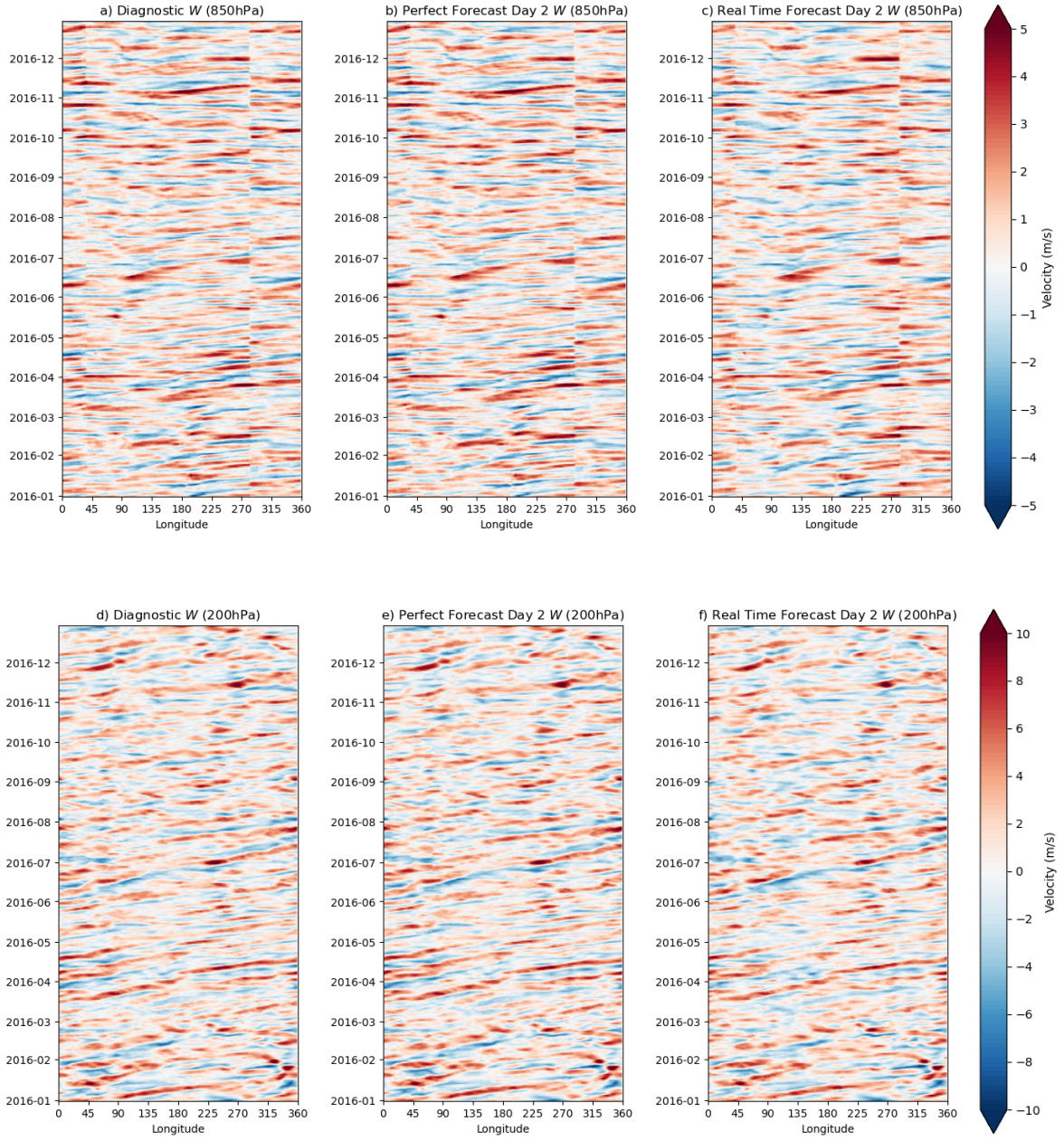

Figure 12: Hovmöller diagrams showing the propagation of Kelvin waves for the year 2016. Top row: 850hPa. Bottom row: 200hPa. Left column: diagnostic dataset. Middle column: perfect forecast dataset. Right column: real-time forecast dataset. The colorbar corresponds to $W(t, \lambda)$, a proxy for the velocity of the Kelvin waves in m/s and thus, dark red indicates wave crests and dark blue wave troughs.

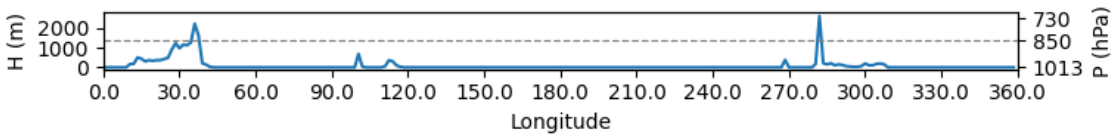

Figure 13: Surface elevation at the equator (0^o latitude). Data retrieved from ECMWF.

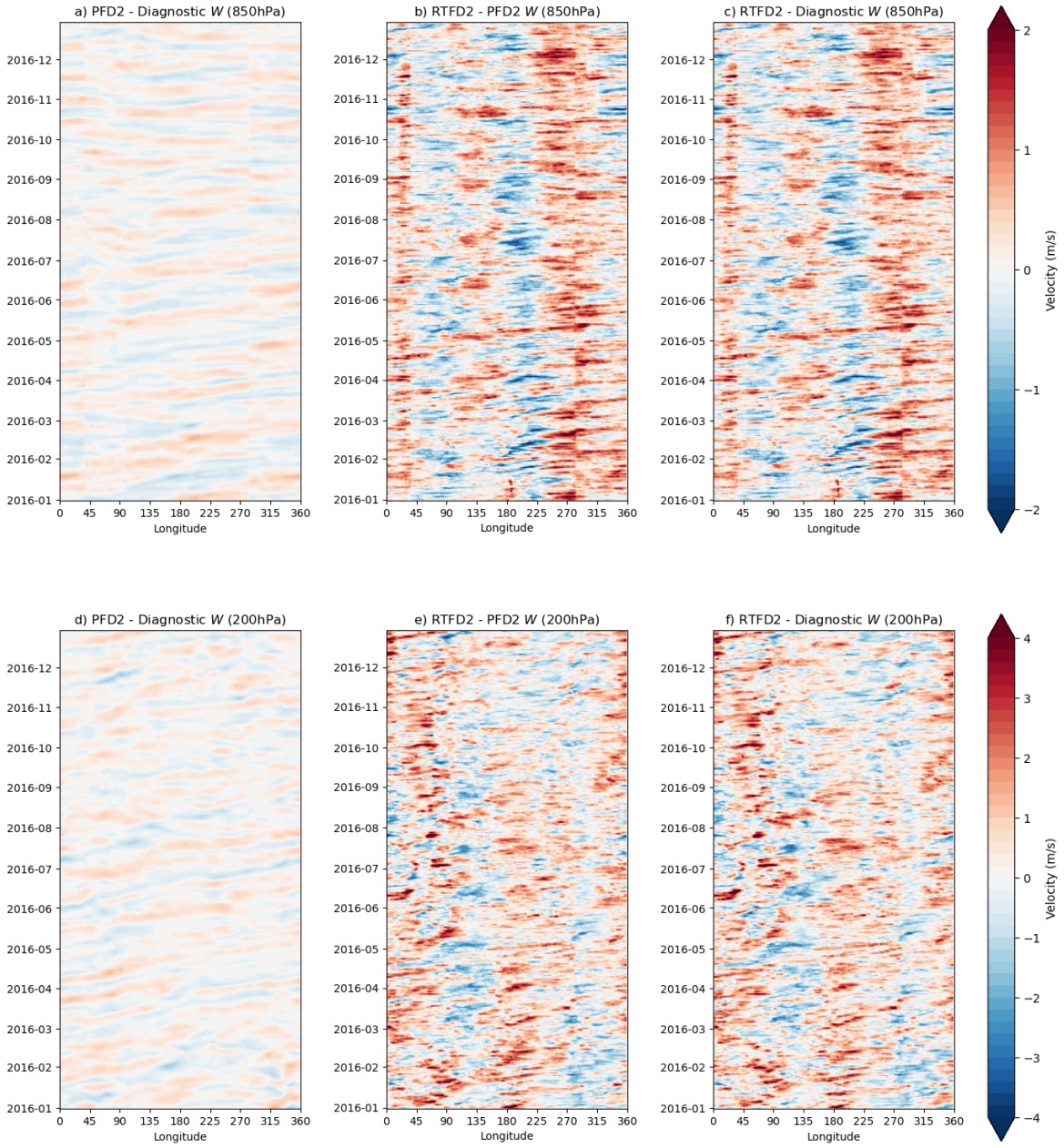

Figure 14: Difference between Hovmöller diagrams of Kelvin waves corresponding to different window types, in the year 2016. Top row: 850hPa. Bottom row: 200hPa. Left column: difference between perfect forecast lead day 2 and diagnostic dataset. Middle column: difference between real-time forecast lead day 2 and perfect forecast lead day 2. Right column: difference between real-time forecast lead day 2 and diagnostic dataset. The colorbar corresponds to the difference in $W(t, \lambda)$, a proxy for the velocity of Kelvin waves in m/s. Note that the scale of the colorbars is distinct from Figure 12.

A more precise visualization of wave propagation at specific longitudes is obtained through the amplitude-phase diagrams shown in Figure 15. In this case the angle coordinate is the phase $\gamma(t, \lambda)$ and the radial coordinate is the amplitude $A(t, \lambda)$. Whereas information on broader spacial and time scales, as given by the Hovmöller plots, is lost, more accurate insight about the direction of propagation and vertical coupling of the waves is gained using these amplitude-phase diagrams. Figure 15 shows a Kelvin wave passing through 0°E travelling eastwards from 20 April 2016 until 30 April 2016. The wave appears to be coupled as it can be identified at both 850hPa (Figure 15 (a)) and 200hPa (Figure 15 (b)) and, at least for days 0-3 and 8-10 convergence at 850hPa corresponds to divergence at 200hPa or vice-versa, which is in accordance with the linear theory of CCEWs. The blue lines indicate the wave as identified in the perfect forecast dataset and the red lines correspond to the wave in the real-time forecast dataset. Up until day 4, at 850hPa, the model simulates the amplitude of the KWs to be too weak and their propagation to be too fast. Afterwards, both peak amplitude and decay of the KWs is prematurely predicted by the model. On the other hand, at 200hPa the phase of the wave is well simulated by the forecast model and on average so is the amplitude, apart from days 6-8 when the model simulates the amplitude of the KWs to be too strong. Note that the plots in Figure 15 were made using $A(t, \lambda)$ instead of $W(t, \lambda)$. This is because the theoretical structure of the Kelvin modes (e.g. Figure 1) dictates that pure divergence/convergence zones would yield zero values for the $W(t, \lambda)$ amplitudes, which would make KW propagation hard to track using $W(t, \lambda)$ in the amplitude-phase plots.

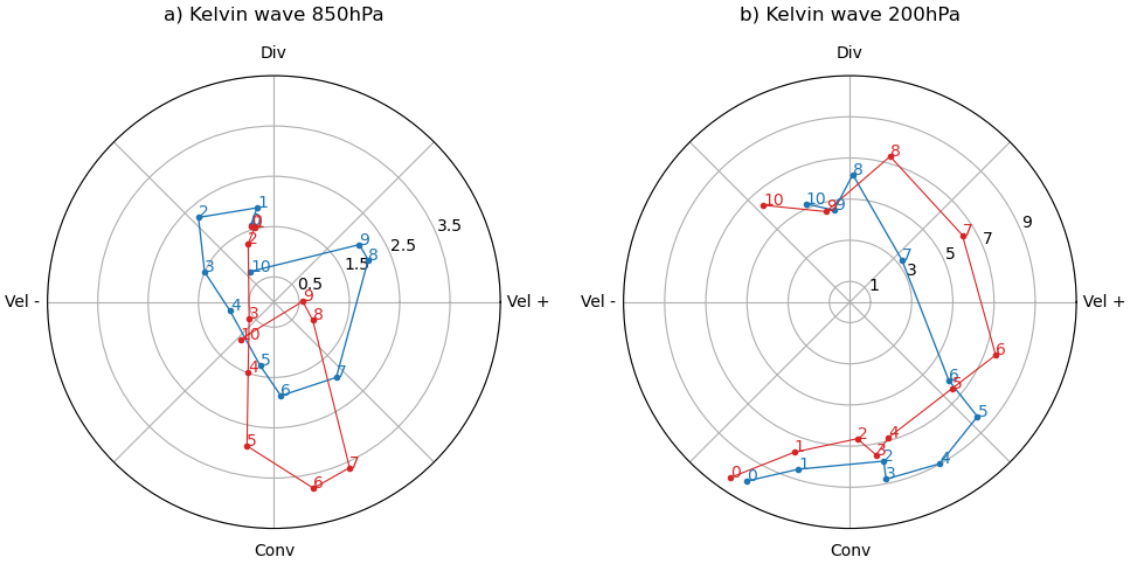

Figure 15: Amplitude-phase diagram of Kelvin waves at a) 850hPa and b) 200hPa. The waves are identified at longitude 0ºE and lead day 0 corresponds to 20 April 2016. Blue lines correspond to the perfect forecast dataset. Red lines corresponds to the real-time forecast dataset. Coloured numbers indicate the lead day of the forecast. Numbers in black indicate the amplitude $A(t, \lambda)$ given in m/s. In the calculation of the amplitude $A(t, \lambda)$ the divergence field $\frac{\partial W}{\partial \lambda}$ was normalized to be in the same range as the wave amplitude $W(t, \lambda)$.

4.2 Model Error and Edge Effects

To quantify the importance of the two error types, namely, the error arising from the frequency filter and the error from the model, we now study the RMSE related to the amplitude $W(t, \lambda)$ and phase $\gamma(t, \lambda)$ of the waves. Figure 16 (a) shows the $W(t, \lambda)$ RMSE for each forecast lead day and Figure 16 (b) shows the same for $\gamma(t, \lambda)$. We will comment them together as they show very similar results. In both cases solid lines correspond to 850hPa and dashed lines to 200hPa. In blue is the RMSE of the perfect forecast dataset when compared to the diagnostic dataset. As such, it exhibits the edge effects

arising from the frequency filter. In green we have the RMSE of the real-time forecast dataset when compared to the perfect-forecast dataset. This shows model error. For all lead days the edge effects are much smaller than the model error. Furthermore, in red is the RMSE of the real-time forecast when compared to the diagnostic dataset, showing both model error and edge effects. It is seen that up until lead day 7 the green and red lines almost overlap. They only bifurcate at day 7. Thus, up until day 7 model error is the most important error type in the real-time forecast dataset with edge effects being negligible. Edge effects become relevant in the real-time forecast for days 7-10.

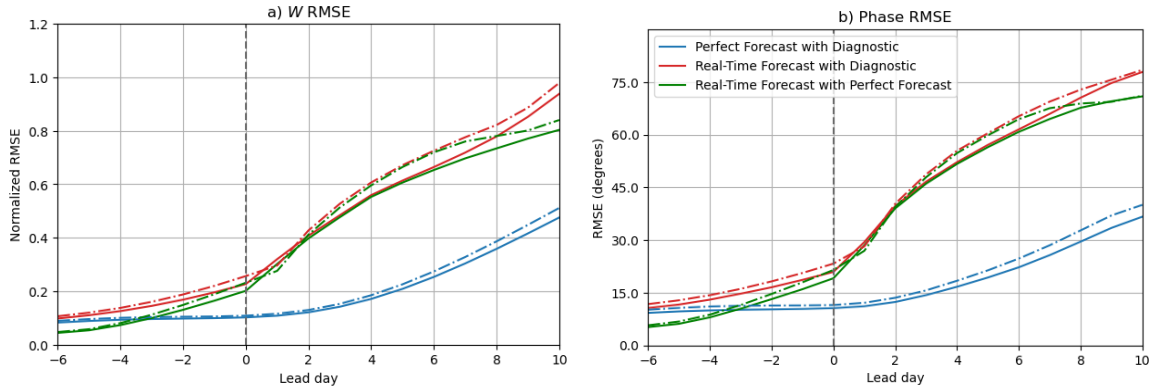

Figure 16: a) Normalized $W(t,\lambda)$ RMSE per forecast lead day. RMSE is normalized using one standard deviation in the diagnostic dataset for the blue and red lines and using one standard deviation in the perfect forecast dataset for the green lines. b) $\gamma(t,\lambda)$ RMSE per forecast lead day. Blue lines correspond to the RMSE of the perfect forecast compared to the diagnostic dataset. Green lines correspond to the RMSE of the real-time forecast compared to the perfect forecast dataset. Red lines correspond to the RMSE of the real-time forecast compared to the diagnostic dataset. Solid lines are for 850hPa and dashed lines for 200hPa.

Now, in Figure 17 the difference in the time averaged wave amplitude $\overline{W}(\lambda)$ between distinct window types is presented for different lead days. By studying this difference at each longitude, the aim is to understand whether the frequency filter or the model show any bias at specific longitudes when reproducing Kelvin waves. The left column of Figure 17 always shows the results for the 850hPa pressure level. The right column corresponds to results regarding the 200hPa pressure level. The different colored lines are for different forecast lead days. Figures 17 (a)-(b) correspond to the $\overline{W}(\lambda)$ difference between the perfect forecast and the diagnostic dataset. As can be seen, the difference is nearly zero for all the lead days shown, and thus, it can be concluded that there is no significant longitudinal bias associated to the edge effects in the frequency filter. On the other hand, Figures 17 (c)-(d) are for the $\overline{W}(\lambda)$ difference between the real-time and the perfect forecast. In this case, the difference is not approximately zero, indicating a bias in the model when representing Kelvin waves over certain longitudes. In particular, the model simulates the amplitude of the KWs to be either too weak or too strong (depending on the lead day) over two regions: Eastern Africa and the Indian Ocean (20°E-80°E) and the Pacific Ocean and Central America (180°E-320°E). This bias is much more pronounced at 850hPa, where the magnitude of the difference exceeds 30% of a standard deviation, when compared to 200hPa, where the magnitude of the difference barely reaches 20% of a standard deviation. The fact that Figures 17 (c)-(d) are almost equivalent to Figures 17 (e)-(f) is another way of visualizing that there is no considerable bias related to the edge effects.

Figure 18 is the same as Figure 17 only for the time mean phase $\overline{\gamma}(\lambda)$. The results are very similar to those extracted from Figure 17. Figures 18 (a)-(b) reveal very little edge effects. The edge effects more closely resemble small magnitude noise than any discernible bias pattern in the frequency filter. Figures 18 (c)-(d) again show model bias over Eastern Africa and the Indian Ocean (20°E-80°E) and over the Pacific Ocean and Central America (180°E-320°E), at both pressure levels, where KWs are simulated by the model either as too fast or too slow (depending on the lead day) and the time av-

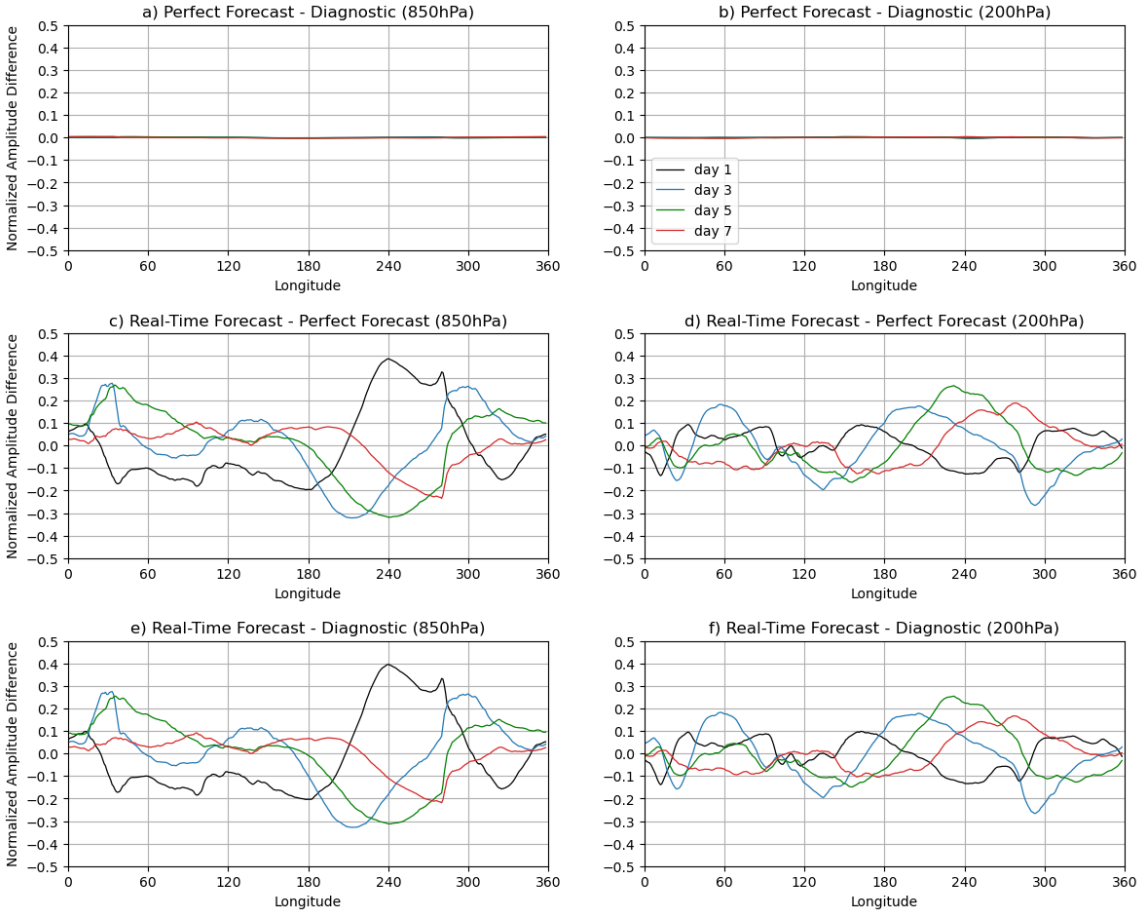

Figure 17: Normalized difference in the time mean wave amplitude $\overline{W}(\lambda)$ for each longitude. Top row: normalized $\overline{W}(\lambda)$ difference between perfect forecast and diagnostic dataset. The difference is normalized according to one standard deviation in the diagnostic dataset. Middle row: normalized $\overline{W}(\lambda)$ difference between real-time forecast and perfect forecast. The difference is normalized according to one standard deviation in the perfect-forecast dataset. Bottom row: normalized $\overline{W}(\lambda)$ difference between real-time forecast and diagnostic dataset. The difference is normalized according to one standard deviation in the diagnostic dataset. Left column: 850hPa. Right column: 200hPa. The different colored lines correspond to different forecast lead days.

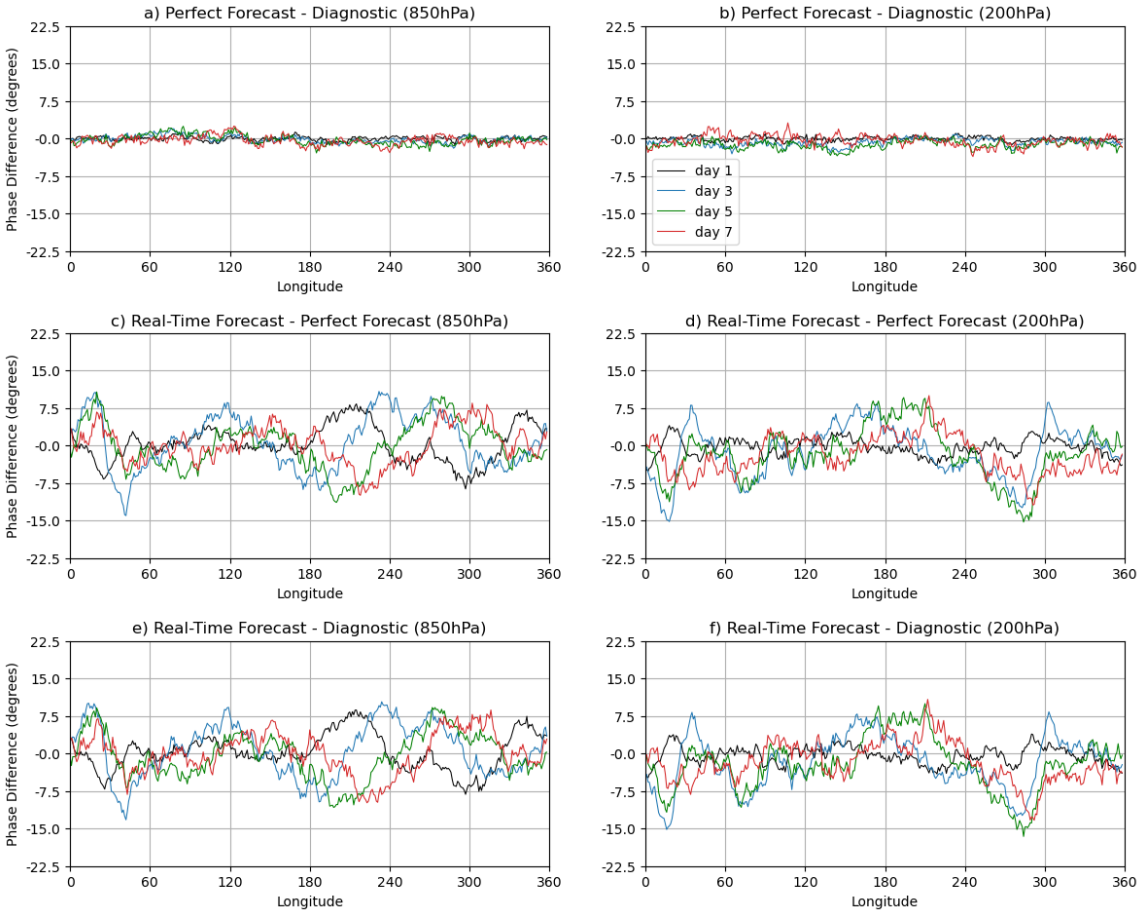

Figure 18: Difference in the time mean wave phase $\overline{\gamma}(\lambda)$ for each longitude. Top row: $\overline{\gamma}(\lambda)$ difference between perfect forecast and diagnostic dataset. Middle row: $\overline{\gamma}(\lambda)$ difference between real-time forecast and perfect forecast. Bottom row: $\overline{\gamma}(\lambda)$ difference between real-time forecast and diagnostic dataset. Left column: 850hPa. Right column: 200hPa. The different colored lines correspond to different forecast lead days.

eraged phase difference can reach absolute values as high as 15°. Unlike what happened for the time mean wave amplitude $\overline{W}(\lambda)$ in Figure 17, the bias in the phase is not more pronounced at 850hPa than at the 200hPa pressure level. Finally, Figures 18 (c)-(d) resemble Figures 18 (e)-(f) confirming that there is no significant bias related to the edge effects of the frequency filter.

Figures similar to Figure 17 and Figure 18, but for the lead day instead of longitude, do not reveal any model or frequency filter bias associated to forecast lead day and, therefore, are not shown.

4.3 Model Bias Interpretation and Correction

We now proceed to physically interpret the bias found over the two longitude regions. Referring back to Figure 13, we see that the high altitude regions are located within the regions where the bias is most pronounced: the East African Mountains are in Eastern Africa and the Andes are in Central America. Furthermore, it would help explain why the bias is more strongly present at 850hPa for the wave amplitude $W(t, \lambda)$. Moreover, according to linear wave theory, topographic waves develop with a similar wavenumber to that of the topography (Gill, 1982a). From Figure 19 we see that the topography is associated to low zonal wavenumbers, with the highest magnitude coefficients corresponding wavenumbers 1-4 and wavenumbers 5-7 still being associated to considerably high coefficients. Then, if we turn our attention to Figure 20, we see that it is mostly waves with wavenumbers 1-3 that have their amplitude and phase misrepresented by the model at 850hPa, with wavenumbers 4 and 5 also being affected for lead day 3 of the phase.

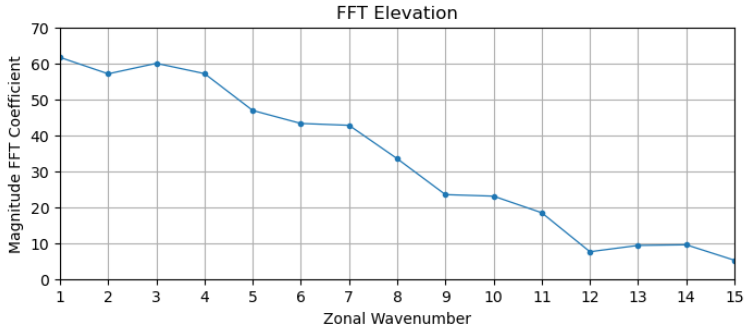

Figure 19: Magnitude FFT coefficients of the average surface elevation in the equatorial band $15^\circ S$-$15^\circ N$. *The average was taken in the meridional direction and the FFT was applied in the zonal direction.*

Additionally, Figure 21 shows a similar behaviour at 200hPa to the one seen at 850hPa in Figure 20, but with much smaller values for the difference in time mean amplitude $\overline{W}(\lambda)$. For the time averaged amplitude $\overline{W}(\lambda)$ it is again wavenumbers 1-3 that are mostly affected, only with day 3 also showing some error associated to wavenumbers 4 and 5. In the case of the time averaged phase $\overline{\gamma}(\lambda)$, day 1 barely shows any bias, as expected from Figures 18 (d) and (f). Days 3 and 5 show bias to be prevalent up to wavenumber 7, which, as previously mentioned, are still associated to FFT coefficients of the elevation with considerable magnitude (Figure 19). Day 7 mostly shows bias in wavenumbers 1-3. In sum, for both amplitude and phase, and for both pressure levels, the zonal wavenumbers corresponding to the bias match the wavenumbers associated to the topography. Therefore, we suggest that the longitudinal bias found in the ECMWF operational forecast is associated to a misrepresentation by the model of the role of topography in the development and propagation of Kelvin waves. Note that from linear wave theory, it is to be expected that a topography induced bias be visible at altitude levels where topography does not reach, as topographic waves can vertically propagate in the atmosphere (Holton, 1973; Gill, 1982a).

This topography related bias in the model could have practical consequences when it comes to the

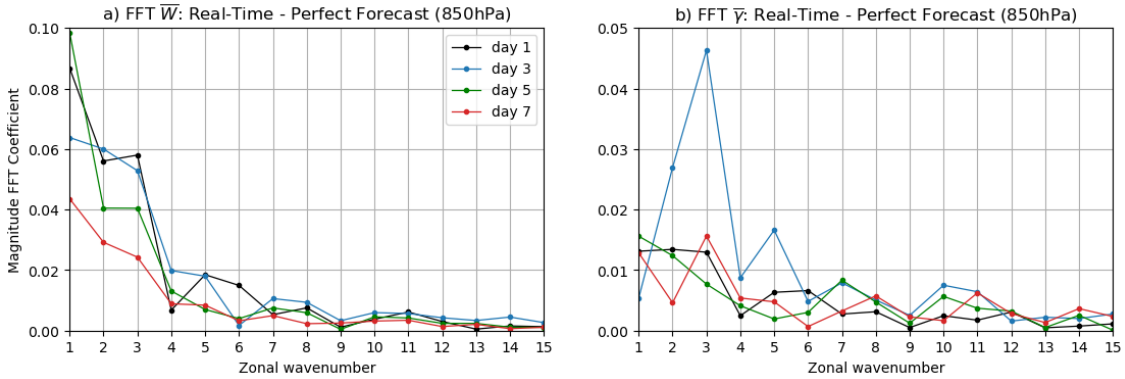

Figure 20: a) FFT coefficients of the difference in the time averaged wave amplitude $\overline{W}(\lambda)$ between real-time forecast and perfect forecast datasets in the zonal direction for 850hPa. b) FFT coefficients of the difference in the time averaged wave phase $\overline{\gamma}(\lambda)$ between real-time forecast and perfect forecast datasets in the zonal direction for 850hPa. Different colored lines correspond to different forecast lead days.

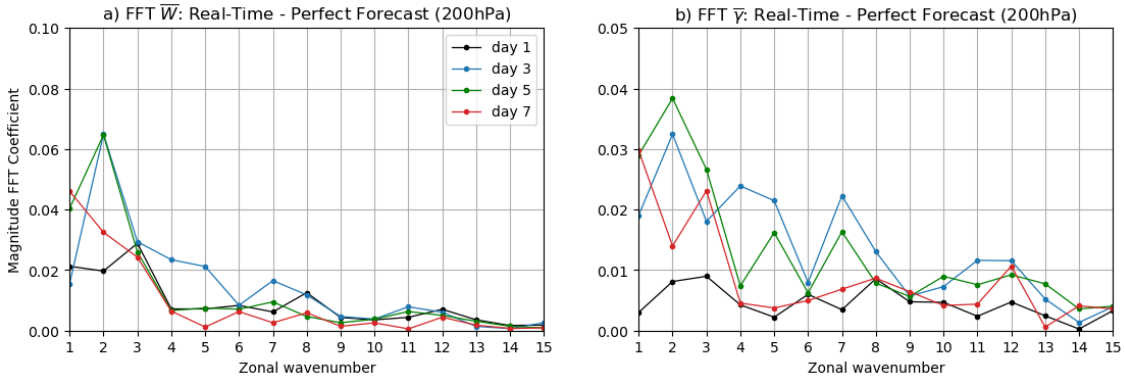

Figure 21: Same as Figure 20 but for the 200hPa pressure level.

predictions of the operational forecast model being studied. Recall that these Kelvin waves could be convectively coupled. We have found that Kelvin waves are represented as too strong (too weak) by the model over some regions. Then one potential consequence of this topography related bias could be that cloud coverage and rainfall over these regions is predicted to be too intense (too weak). Also, the model simulates the Kelvin waves to propagate too fast (too slow) around those same areas. Thus, the bias could also cause problems in the forecast of rainfall patterns in general and even monsoon season onsets in particular, as they may be predicted to arrive too early (too late).

As we want this method to be usable in a real-time operational context, we introduce a way in which to correct the model bias. This can be done by removing the 30-day running average throughout the years 2015-2017 for each forecast lead day of the wave amplitude $W(t, \lambda)$ of the real-time forecast dataset. The results are shown in Figure 22. The top row corresponds to the results for the time mean wave amplitude $\overline{W}(\lambda)$ and the bottom row is for the time mean wave phase $\overline{\gamma}(\lambda)$. The left column is for 850hPa and the right for 200hPa. It is seen in Figures 22 (a)-(b) that the model bias related to the wave amplitude in the real-time forecast dataset has been removed as the difference in $\overline{W}(\lambda)$ between the real-time and perfect forecast datasets is approximately zero at every longitude. By turning our attention to Figures 22 (c)-(d) we notice that the bias in the wave phase of the real-time forecast has been greatly reduced when compared to the uncorrected phase seen in Figures 18 (c)-(d). Nevertheless, the topography induced model bias is not as close to zero for the phase as it was for the wave amplitude $W(t, \lambda)$. To explain this discrepancy we take the derivative over λ of the form of the

horizontal solutions $\mathbf{W}^{\alpha}_{kn}$, given by Equation (22), which yields

$$\frac{\partial \mathbf{W}^{\alpha}_{kn}}{\partial \lambda} = e^{-i\sigma^{\alpha}_{nk}\, t} ike^{ik\lambda} \mathbf{\Theta}^{\alpha}_{kn}. \tag{38}$$

The factor ik in Equation (38) has as a result that the larger the zonal wavenumber of the wave, the larger the value of the mass divergence field of that wave. Now, the mass divergence field $\frac{\partial \mathbf{W}}{\partial \lambda}$ constitutes the imaginary part of the complex variable $I(t, \lambda)$ used to calculate the phase $\gamma(t, \lambda)$ (Equations (36) and (37)). On the other hand, the mass divergence field $\frac{\partial \mathbf{W}}{\partial \lambda}$ is not included in the wave amplitude $W(t, \lambda)$. The fact that high zonal wavenumbers, with appreciable magnitude, are indeed present in Figures 22 (c)-(d) and not in Figures 22 (a)-(b), then suggest that the mass divergence field is a key contributor to the bias corrected phase not being as close to zero as the bias corrected amplitude.

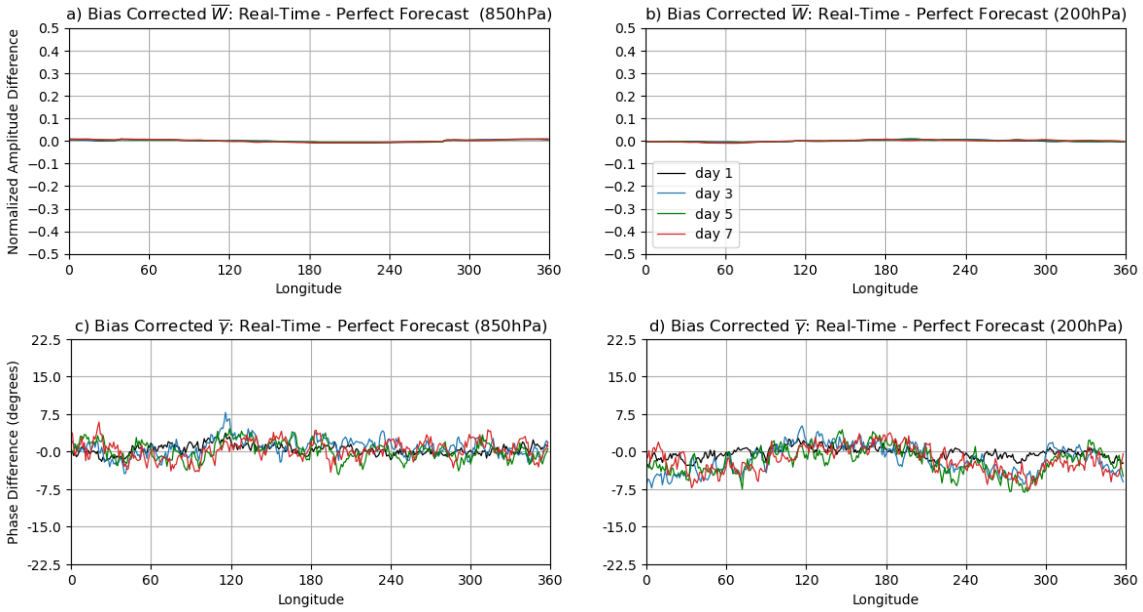

Figure 22: Top row: time mean difference between real-time and perfect forecast $\overline{W}(\lambda)$ with bias corrected $W(t, \lambda)$ for the real-time forecast dataset. Bottom row: difference between real-time and perfect forecast phase $\overline{\gamma}(\lambda)$ with bias corrected $W(t, \lambda)$ for the real-time dataset in the computation of $I(t, \lambda)$ and subsequent calculation of $\gamma(t, \lambda)$. Left column: 850hPa. Right column: 200hPa. The topography related bias present in the real-time forecast wave amplitude $W(t, \lambda)$ is corrected by removing the 30-day moving average throughout 2015-2017 for each forecast lead day starting at lead day 0.

5 Conclusion

In this thesis, a methodology for the local identification of equatorial Kelvin waves in real-time operational weather forecasts was developed. The identification consists in the application of one linear operation to the data, i.e. the projection of the data onto the Hough structure of a single Kelvin mode. On top of that, a frequency-wavenumber filter may be applied. As such, the method requires very low computational cost when compared to the other projection methods found in the literature, namely 2D-PCFs, 3D-NMFs and the 2D-NMFs method recently developed by Castanheira and Marques (2023). Additionally, since the multivariate structure of the Hough vector functions is used, the Kelvin waves are univocally identified and there is no need to pre-filter the data between eastward and westward moving disturbances, as in the univariate projection method onto 2D-PCFs. Furthermore, the novel local identification method shows low sensitivity to the choice of both the equivalent depth parameter h_e and the zonal wavenumber k of the Kelvin mode onto which the data is projected.

Then, by applying the developed methodology to the 2015-2017 ECMWF operational forecast model, a topography related bias, which affects both the amplitude and phase of the Kelvin waves, was found. This could have practical consequences for the forecasts of the ECMWF operational forecast model, as it may potentially introduce errors in the simulated intensity and timing of a variety of equatorial atmospheric phenomena, namely cloud coverage, rainfall and the onset of summer monsoons.

References

Castanheira, J. M. and Marques, C. A. F. (2015). Convectively coupled equatorial-wave diagnosis using three-dimensional normal modes. *Quarterly Journal of the Royal Meteorological Society*, 141(692):2776–2792. _eprint: https://onlinelibrary.wiley.com/doi/pdf/10.1002/qj.2563.

Castanheira, J. M. and Marques, C. A. F. (2021). The equatorial wave skeleton of the Madden–Julian Oscillation. *Quarterly Journal of the Royal Meteorological Society*, 147(740):3778–3788. _eprint: https://onlinelibrary.wiley.com/doi/pdf/10.1002/qj.4156.

Castanheira, J. M. and Marques, C. A. F. (2023). Identification of equatorial waves using Hough function vectors. *Quarterly Journal of the Royal Meteorological Society*, page qj.4459.

Chang, C.-P. (1970). Westward Propagating Cloud Patterns in the Tropical Pacific as seen from Time-Composite Satellite Photographs. *Journal of the Atmospheric Sciences*, 27(1):133–138. Publisher: American Meteorological Society Section: Journal of the Atmospheric Sciences.

Daley, R. (1993). *Atmospheric Data Analysis*. Cambridge University Press. Google-Books-ID: RHM6pTMRTHwC.

Duchon, C. E. (1979). Lanczos Filtering in One and Two Dimensions. *Journal of Applied Meteorology and Climatology*, 18(8):1016–1022. Publisher: American Meteorological Society Section: Journal of Applied Meteorology and Climatology.

Ferrett, S., Yang, G.-Y., Woolnough, S. J., Methven, J., Hodges, K., and Holloway, C. E. (2020). Linking extreme precipitation in Southeast Asia to equatorial waves. *Quarterly Journal of the Royal Meteorological Society*, 146(727):665–684. _eprint: https://onlinelibrary.wiley.com/doi/pdf/10.1002/qj.3699.

Flatau, M. K., Flatau, P. J., Schmidt, J., and Kiladis, G. N. (2003). Delayed onset of the 2002 Indian monsoon. *Geophysical Research Letters*, 30(14). _eprint: https://onlinelibrary.wiley.com/doi/pdf/10.1029/2003GL017434.

Gehne, M. and Kleeman, R. (2012). Spectral Analysis of Tropical Atmospheric Dynamical Variables Using a Linear Shallow-Water Modal Decomposition. *Journal of the Atmospheric Sciences*, 69(7):2300–2316. Publisher: American Meteorological Society Section: Journal of the Atmospheric Sciences.

Gill, A. E. (1982a). *Atmosphere-Ocean Dynamics*. Academic Press.

Gill, A. E. (1982b). Studies of moisture effects in simple atmospheric models: The stable case. *Geophysical & Astrophysical Fluid Dynamics*, 19(1-2):119–152. Publisher: Taylor & Francis _eprint: https://doi.org/10.1080/03091928208208950.

Hamming, R. W. R. W. (1983). *Digital filters*. Englewood Cliffs, NJ : Prentice-Hall.

Holton, J. R. (1973). *An Introduction to Dynamic Meteorology*. American Association of Physics Teachers.

Holton, J. R. and Lindzen, R. S. (1972). An Updated Theory for the Quasi-Biennial Cycle of the Tropical Stratosphere. *Journal of the Atmospheric Sciences*, 29(6):1076–1080. Publisher: American Meteorological Society Section: Journal of the Atmospheric Sciences.

Hough, S. S. (1897). On the application of harmonic analysis to the dynamical theory of the tides. Part I. On Laplace's 'oscillations of the first species,' and on the dynamics of ocean currents. *Proceedings of the Royal Society of London*, 61(369-377):236–238. Publisher: Royal Society.

Hough, S. S. (1898). On the application of harmonic analysis to the dynamical theory of the tides. Part II. On the general integration of Laplace's dynamical equations. *Proceedings of the Royal Society of London*, 62(379-387):209–210. Publisher: Royal Society.

Kasahara, A. (1976). Normal Modes of Ultralong Waves in the Atmosphere. *Monthly Weather Review*, 104(6):669–690. Publisher: American Meteorological Society Section: Monthly Weather Review.

Kasahara, A. (1980). Effect of Zonal Flows on the Free Oscillations of a Barotropic Atmosphere. *Journal of the Atmospheric Sciences*, 37(5):917–929. Publisher: American Meteorological Society Section: Journal of the Atmospheric Sciences.

Kasahara, A. and Puri, K. (1981). Spectral Representation of Three-Dimensional Global Data by Expansion in Normal Mode Functions. *Monthly Weather Review*, 109(1):37–51. Publisher: American Meteorological Society Section: Monthly Weather Review.

Kiladis, G. N., Wheeler, M. C., Haertel, P. T., Straub, K. H., and Roundy, P. E. (2009). Convectively coupled equatorial waves. *Reviews of Geophysics*, 47(2). _eprint: https://onlinelibrary.wiley.com/doi/pdf/10.1029/2008RG000266.

Lawton, Q. A. and Majumdar, S. J. (2023). Convectively Coupled Kelvin Waves and Tropical Cyclogenesis: Connections through Convection and Moisture. *Monthly Weather Review*, 151(7):1647–1666. Publisher: American Meteorological Society Section: Monthly Weather Review.

Liberato, M. L. R., Castanheira, J. M., Torre, L. d. l., DaCamara, C. C., and Gimeno, L. (2007). Wave Energy Associated with the Variability of the Stratospheric Polar Vortex. *Journal of the Atmospheric Sciences*, 64(7):2683–2694. Publisher: American Meteorological Society Section: Journal of the Atmospheric Sciences.

Longuet-Higgins, M. S. (1968). The eigenfunctions of Laplace's tidal equation over a sphere. *Philosophical Transactions of the Royal Society of London. Series A, Mathematical and Physical Sciences*, 262(1132):511–607. Publisher: Royal Society.

Marques, C. A. F. and Castanheira, J. M. (2018). Diagnosis of Free and Convectively Coupled Equatorial Waves. *Mathematical Geosciences*, 50(5):585–606.

Marques, C. A. F., Marta-Almeida, M., and Castanheira, J. M. (2020). Three-dimensional normal mode functions: open-access tools for their computation in isobaric coordinates (p-3DNMF.v1). *Geoscientific Model Development*, 13(6):2763–2781. Publisher: Copernicus GmbH.

Matsuno, T. (1966). Quasi-Geostrophic Motions in the Equatorial Area. *Journal of the Meteorological Society of Japan. Ser. II*, 44(1):25–43.

Mounier, F., Kiladis, G. N., and Janicot, S. (2007). Analysis of the Dominant Mode of Convectively Coupled Kelvin Waves in the West African Monsoon. *Journal of Climate*, 20(8):1487–1503. Publisher: American Meteorological Society Section: Journal of Climate.

Plumb, R. A. (1977). The Interaction of Two Internal Waves with the Mean Flow: Implications for the Theory of the Quasi-Biennial Oscillation. *Journal of the Atmospheric Sciences*, 34(12):1847–1858. Publisher: American Meteorological Society Section: Journal of the Atmospheric Sciences.

Roundy, P. E. (2020). Interpretation of the spectrum of eastward-moving tropical convective anomalies. *Quarterly Journal of the Royal Meteorological Society*, 146(727):795–806. _eprint: https://onlinelibrary.wiley.com/doi/pdf/10.1002/qj.3709.

Stephan, C. C., Žagar, N., and Shepherd, T. G. (2021). Waves and coherent flows in the tropical atmosphere: New opportunities, old challenges. *Quarterly Journal of the Royal Meteorological Society*, 147(738):2597–2624. _eprint: https://onlinelibrary.wiley.com/doi/pdf/10.1002/qj.4109.

Swarztrauber, P. N. and Kasahara, A. (1985). The Vector Harmonic Analysis of Laplace's Tidal Equations. *SIAM Journal on Scientific and Statistical Computing*, 6(2):464–491. Publisher: Society for Industrial and Applied Mathematics.

Takayabu, Y. (1994a). Large-Scale Cloud Disturbances Associated with Equatorial Waves: Part I: Spectral Features of the Cloud Disturbances. *Journal of the Meteorological Society of Japan*, 72:433–449.

Takayabu, Y. (1994b). Large-Scale Cloud Disturbances Associated with Equatorial Waves: Part II: Westward-Propagating Inertio-Gravity Waves. *Journal of the Meteorological Society of Japan. Ser. II*, 72:451–465.

Tanaka, H. (1985). Global Energetics Analysis by Expansion into Three-Dimensional Normal Mode Functions during the FGGE Winter. *Journal of the Meteorological Society of Japan. Ser. II*, 63(2):180–200.

Tanaka, H. L. and Kung, E. C. (1988). Normal Mode Energetics of the General Circulation during the FGGE Year. *Journal of the Atmospheric Sciences*, 45(23):3723–3737. Publisher: American Meteorological Society Section: Journal of the Atmospheric Sciences.

Vogel, P., Knippertz, P., Fink, A. H., Schlueter, A., and Gneiting, T. (2020). Skill of Global Raw and Postprocessed Ensemble Predictions of Rainfall in the Tropics. *Weather and Forecasting*, 35(6):2367–2385. Publisher: American Meteorological Society Section: Weather and Forecasting.

Wallace, J. M. (1971). Spectral studies of tropospheric wave disturbances in the tropical western Pacific. *Reviews of Geophysics*, 9(3):557.

Wallace, J. M. and Kousky, V. E. (1968). Observational Evidence of Kelvin Waves in the Tropical Stratosphere. *Journal of the Atmospheric Sciences*, 25(5):900–907. Publisher: American Meteorological Society Section: Journal of the Atmospheric Sciences.

Wang, L., Li, T., and Nasuno, T. (2018). Impact of Rossby and Kelvin Wave Components on MJO Eastward Propagation. *Journal of Climate*, 31(17):6913–6931. Publisher: American Meteorological Society Section: Journal of Climate.

Webster, P. J. (2020). *Dynamics of the Tropical Atmosphere and Oceans*.

Wheeler, M. and Kiladis, G. N. (1999). Convectively Coupled Equatorial Waves: Analysis of Clouds and Temperature in the Wavenumber–Frequency Domain. *Journal of the Atmospheric Sciences*, 56(3):374–399.

Wong, M. L. M. (2009). Wavelet Analysis of the Convectively Coupled Equatorial Waves in the Wavenumber–Frequency Domain. *Journal of the Atmospheric Sciences*, 66(1):209–212. Publisher: American Meteorological Society Section: Journal of the Atmospheric Sciences.

Yanai, M. and Maruyama, T. (1966). Stratospheric Wave Disturbances Propagating over the Equatorial Pacific. *Journal of the Meteorological Society of Japan. Ser. II*, 44(5):291–294.

Yang, G.-Y., Ferrett, S., Woolnough, S., Methven, J., and Holloway, C. (2021). Real-Time Identification of Equatorial Waves and Evaluation of Waves in Global Forecasts. *Weather and Forecasting*, 36(1):171–193. Publisher: American Meteorological Society Section: Weather and Forecasting.

Yang, G.-Y., Hoskins, B., and Slingo, J. (2003). Convectively Coupled Equatorial Waves: A New Methodology for Identifying Wave Structures in Observational Data. *Journal of the Atmospheric Sciences*, 60(14):1637–1654. Publisher: American Meteorological Society Section: Journal of the Atmospheric Sciences.

Yang, G.-Y., Hoskins, B., and Slingo, J. (2007). Convectively Coupled Equatorial Waves. Part I: Horizontal and Vertical Structures. *Journal of the Atmospheric Sciences*, 64(10):3406–3423. Publisher: American Meteorological Society Section: Journal of the Atmospheric Sciences.

Yang, G.-Y., Slingo, J., and Hoskins, B. (2009). Convectively Coupled Equatorial Waves in High-Resolution Hadley Centre Climate Models. *Journal of Climate*, 22(8):1897–1919. Publisher: American Meteorological Society Section: Journal of Climate.

Yessad, K. (2015). FULL-POS in the cycle 46t1r1 of ARPEGE/IFS. *Meteo-France/CNRM Technical Notes*.

Žagar, N., Andersson, E., and Fisher, M. (2005). Balanced tropical data assimilation based on a study of equatorial waves in ECMWF short-range forecast errors. *Quarterly Journal of the Royal Meteorological Society*, 131(607):987–1011.

Žagar, N., Tribbia, J., Anderson, J. L., and Raeder, K. (2009). Uncertainties of Estimates of Inertia–Gravity Energy in the Atmosphere. Part II: Large-Scale Equatorial Waves. *Monthly Weather Review*, 137(11):3858–3873. Publisher: American Meteorological Society Section: Monthly Weather Review.